Causes of large-scale sea level variations in the Southern Ocean: Analyses of sea level and a barotropic model

Frédéric Vivier, Kathryn A. Kelly, Migel Harismendy

Causes of large-scale sea level variations in the Southern Ocean: Analyses of sea level and a barotropic model

Frédéric Vivier

Laboratoire d'Océanographie Dynamique et de Climatologie, Institut Pierre Simon de Laplace, Université Pierre et Marie Curie, Paris, France

Kathryn A. Kelly

Applied Physics Laboratory, University of Washington, Seattle, Washington, USA

Migel Harismendy

Laboratoire d'Océanographie Dynamique et de Climatologie, Institut Pierre Simon de Laplace, Université Pierre et Marie Curie, Paris, France

Received 18 October 2004; revised 7 April 2005; accepted 3 June 2005; published 23 September 2005.

[1] We analyze a decade of sea surface height (SSH) measurements in the Southern Ocean from the TOPEX/Poseidon and ERS altimeters, with a focus on the variability at timescales <2 years. Among the different processes contributing to large-scale SSH variations, the barotropic response to the winds dominates poleward of 50°S, while thermosteric processes dominate equatorward, except for resonant basins for the barotropic modes and regions of intense eddy activity. A finite element barotropic model has been developed to analyze the vorticity budget. The SSH from the model agrees well with observations. The leading barotropic mode, which is annular and is confined near Antarctica, is responsible for most of the barotropic circumpolar transport. It is coherent with the zonally integrated eastward wind stress consistent with a free mode response. Although previously evidenced in bottom pressure data, this mode is only partially seen in altimeter data because of ice coverage. It nevertheless distinctly appears above the Pacific ridges where it expands meridionally up to midlatitudes. In the rest of the domain, several regions coherent with the local wind stress curl are found. These are regions isolated by f/H contours, mostly deep basins. An analysis of the vorticity budget shows that, generally, topographic Sverdrup balance is the leading process for periods $\geq$50 days, but in some regions (resonant basins), diffusive and nonstationary terms are important. A model experiment shows that transients redistribute energy along f/H waveguides, contributing to drain resonant regions, as was hypothesized in previous works.

Citation: Vivier, F., K. A. Kelly, and M. Harismendy (2005), Causes of large-scale sea level variations in the Southern Ocean: Analyses of sea level and a barotropic model, *J. Geophys. Res.*, *110*, C09014, doi:10.1029/2004JC002773.

1. Introduction

[2] With more than a decade of uninterrupted measurements, recent satellite altimetry missions, in particular TOPEX/Poseidon (T/P) and its follow-up, Jason, have demonstrated their capability to monitor sea level variations on a global scale with great accuracy and high spatiotemporal resolution. They have substantially improved our view and understanding of the variability of the ocean on spatial scales ranging from a few tens of kilometers (mesoscale) to several thousand kilometers (large scale) on a wide range of timescales, from daily (e.g., tides) to interannual [e.g., *Fu and Cazenave*, 2001]. The altimeter record is now long enough to provide a comfortable, statistically significant, description of the variability of the sea surface height (SSH) at timescales shorter than 2 years, which is the focus of this study.

[3] The sea level varies under the action of a variety of processes, which can schematically be divided into two categories: changes in sea level that involve a change in the mass of the fluid column on the one hand, and those that involve a volume change at constant mass. At timescales shorter than 2 years, the former include the ocean's barotropic response to the wind-forcing and pressure changes, while the latter include steric changes and baroclinic processes.

[4] Several previous studies have tried to distinguish systematically the dominant processes, be they dynamic or thermodynamic, that contribute to the SSH variations in the T/P record [e.g., *Stammer*, 1997; *Fukumori et al.*, 1998; *Vivier et al.*, 1999, hereinafter referred to as VKT99].

0148-0227/05/2004JC002773

Focusing on the Pacific Ocean, VKT99 showed that the dominant processes affecting sea surface height variability vary regionally: baroclinic Rossby waves, steric response to seasonal heating, and the response to wind stress curl forcing are all important. The steric response to surface heating dominates at midlatitudes, while baroclinic Rossby waves account for >70% of SSH variance between 10°S and 10°N but only ~30% between 10°N and 30°N. A topographic Sverdrup balance is detectable over most of the North Pacific at latitudes as low as 10–15°N, as well as in the South Pacific, where it is seen north of 50°S (confirming early works by *Mestas-Nuñez et al.* [1992] on the basis of Seasat data).

[5] The present study focuses on the Southern Ocean, which is defined here broadly as regions south of 30°S. It has been dramatically undersampled in terms of in situ measurements, compared to the rest of the world ocean, and satellite data are particularly useful there. A strong motivation of our analysis is to be able to distinguish different contributions to the SSH signal, that pertain to different physical processes. For instance steric height changes are primarily influenced by heat exchanges with the atmosphere, and are therefore directly relevant for climate studies. An expected benefit from this analysis is to gain insight in each of the separate contributions, which when added together give a blurred picture of the ocean's response to momentum or buoyancy forcing. In this analysis, we will specifically detail the barotropic vorticity budget.

[6] On the basis of scaling arguments, *Gill and Niiler* [1973] showed that poleward of 30°, the large-scale seasonal ocean response is expected to be barotropic, whereas baroclinic mechanisms dominate equatorward of 30°. Indeed recent analyses of altimeter data have revealed substantial wind-forced barotropic variability in the Southern Ocean [e.g., *Fu and Davidson*, 1995; *Stammer et al.*, 2000]. This response is complex and varies regionally, with for instance 25 day topographic Rossby waves trapped in the Argentine Basin [*Fu et al.*, 2001] or resonant barotropic modes in the Bellingshausen Basin and Australian-Antarctic Basin [*Chao and Fu*, 1995; *Fukumori et al.*, 1998; *Webb and de Cuevas*, 2002a, 2002b; *Fu*, 2003]. According to *Willebrand et al.* [1980], the barotropic ocean's response is dominated by planetary or topographic waves (mostly topographic Rossby waves) at periods between a week and a few months. Beyond monthly timescales (i.e., when a barotropic adjustment has occurred) a time-dependent Sverdrup balance between meridional current and wind stress curl is set up.

[7] Outside of the tropics, as β decreases, a realistic estimate of the barotropic time-varying Sverdrup balance requires consideration of the actual topography of the ocean. *Koblinsky* [1990] claims that including topography in the background potential vorticity (PV) field enhances the effective β by an order of magnitude at midlatitudes. The topographic Sverdrup balance is

$$\mathcal{J}\left(\psi, \frac{f}{H}\right) = \mathrm{curl}\left(\frac{\boldsymbol{\tau}}{\rho_0 H}\right), \qquad (1)$$

where $\mathcal{J}(.,.)$ is the determinant of the Jacobian matrix with respect to x and y, f is the planetary vorticity (Coriolis parameter), H is the ocean depth, $\boldsymbol{\tau}$ is the surface wind stress, ρ_0 is the mean density of the ocean, ψ is the stream function of the depth integrated flow, that is, $\mathbf{k} \times \nabla\psi = \int_{-H}^{0} \mathbf{v} dz$, where $\mathbf{v}$ is the horizontal velocity vector, and $\mathbf{k}$ is a vertical unit vector. Equation (1) simply states that the advection of potential vorticity f/H balances the input of potential vorticity by the winds, or in other words that winds force flows across f/H contours. The validity of the Sverdrup relation is also dependent upon the spatial scales considered, as shown by *Cummins* [1991] with a stochastically forced barotropic QG model of the North Pacific. He found that the topographic Sverdrup balance became evident only over scales larger than 4°.

[8] This simple balance represents the leading dynamics over many regions of the world ocean. For example, VKT99 showed that integration of (1) along its characteristics (f/H contours) can skillfully represent the barotropic seasonal variations of the SSH in the North Pacific. This can be achieved in the North Pacific because nearly all f/H contours intercept the coast, and such a blocking of the contours is essential in allowing a pressure gradient to build up and eventually a Sverdrup balance to be set up.

[9] In the Southern Ocean, the distribution of f/H is evidently more complex, departing greatly from latitude circles because of the dominant influence of topography (Figure 1). The Southern Ocean is the only example of a periodic channel in the world ocean, and a bundle of f/H contours close on themselves near Antarctica (although a significant fraction of the contours are blocked by topography at Drake Passage). Contours are also closed in other places, primarily near midocean ridges, and for such regions higher-order dynamics (e.g., dissipative processes, baroclinic pressure torque, time-dependent dynamics) are necessary to balance the vorticity budget [*Hasselmann*, 1982; *Koblinsky*, 1990]. This is so because the Sverdrup balance prescribes only that component of the flow orthogonal to f/H contours while the other component is essentially a nonlocal response, obtained by integration along f/H contours using the continuity equation. For a closed contour, (1) would force flows inside the enclosed region, which is not compatible with the nondivergence requirement.

[10] In this analysis, we will therefore consider a more detailed vorticity equation for the depth-integrated flow, retaining time-dependent terms as well as bottom friction. The latter is numerically solved over the Southern Ocean during the T/P decade for comparison with altimeter measurements, using a finite element formulation in space, and a spectral approach in time. The model is used to examine spatial variations of the different terms of the vorticity budget.

[11] This study is organized as follows. Altimeter observations together with the surface flux data used to estimate the different contributions to the SSH are described in section 2. Steric and other baroclinic processes are estimated in section 3. In section 4 we present the finite element model developed to estimate the barotropic stream function in a periodic channel such as the Southern Ocean. The analysis of the barotropic variability of the altimeter data is presented in section 5 together with a discussion of the vorticity budget. In particular, we compare the outputs from a run with and without

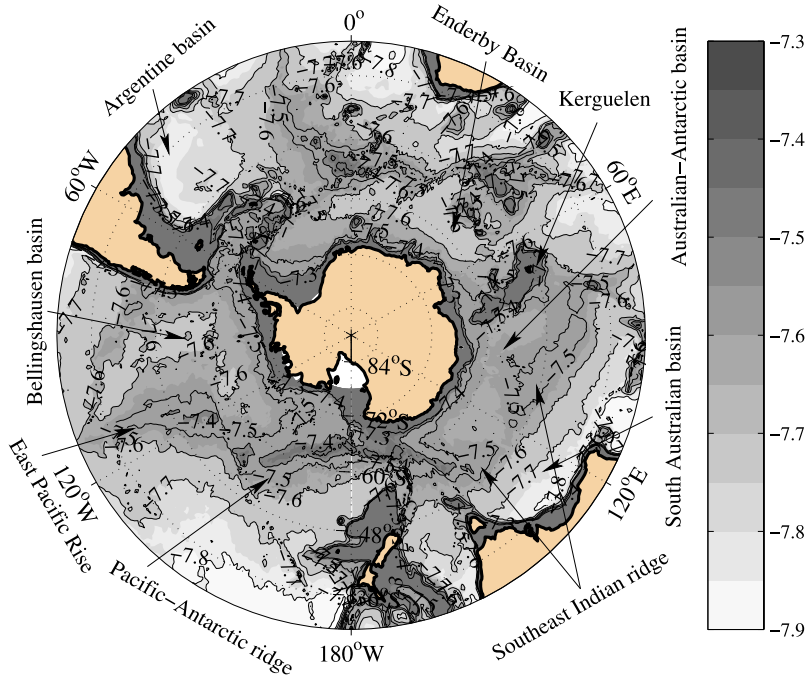

Figure 1. Potential vorticity f/H over the Southern Ocean. Contours of $\log_{10}(-f/H)$ are shown for clarity.

transient terms to highlight regions of energy leakage. The results are summarized in section 6.

2. Altimeter and Surface Flux Data

2.1. Sea Surface Height Observations

[12] We use a ~10 year series (October 1992 to August 2002) of SSH data obtained from a merge between TOPEX/Poseidon (T/P) and ERS (European Remote Sensing satellite) altimeter observations. The TOPEX/Poseidon satellite, launched in August 1992, is a joint US/French project. It measures the sea level above a reference ellipsoid along repeat ground tracks every 9.9 days. In September 2002 T/P was moved to a new orbit halfway between its original ground tracks, while its former tracks are now occupied by Jason-1, both flying in tandem since December 2001. ESA satellites ERS-1 (operational between 1991 and 1996) and its follow-up, ERS-2 (launched in April 1995) have a repeat period of 35 days, except for the period from January 1994 through March 1995 during which ERS1 orbit was changed for geodetic applications.

[13] The merged data we have used are maps of SSH anomaly relative to a 7 year mean (January 1993 to January 1999). They are produced at a 7 day interval by the CLS Space Oceanography Division [*Collecte, Localisation, Satellites*, 2002]. Specific data processing of the T/P Merged Geophysical Data Records (MGDR) included use of the GOT99 tidal correction [*Ray*, 1999], as well as an inverse barometer correction with a variable mean pressure [e.g., *Dorandeu and Le Traon*, 1999]. A global adjustment using T/P as a reference was performed to correct for ERS-1/2 orbit error [*Le Traon et al.*, 1998]. The SSH maps, which are provided on a Mercator 1/3° grid (resolution ranging from 16 to 37 km depending on latitude), were obtained using the mapping method detailed in *Ducet et al.* [2000]. The correlation scales for the objective mapping vary with latitude, ranging from 350 km at the equator to 92 km at 66°S in space, and 15 days in time for the extratropics. As a consequence of this processing there is little energy left at periods shorter than ~40 days.

[14] A pattern of SSH variations in the Southern Ocean (not shown) closely follows the main Antarctic Circumpolar Current (ACC) fronts, namely the Subantarctic Front (SAF) and the Polar Front (PF). It is particularly marked in western boundary regions (East Australian current, Brazil-Malvinas confluence, Aghulas current retroflexion) where the magnitude of SSH variations exceed 30 cm RMS in the last two regions. SSH variations in excess of 10 cm RMS are observed almost everywhere in the SAF, reaching up to 25 cm in the western part of the Indian sector. This variability is mainly associated with meandering (and eddy formation) of two major ACC fronts at mesoscales and zonal migration of the fronts at quasi-annual and interannual scales [e.g., *Rintoul et al.*, 2002]. Major ACC fronts can split into several branches [e.g., *Sokolov and Rintoul*, 2002] so the typical spatial separations of the fronts and fronts' meanders scales are of the order of internal Rossby radius of deformation.

[15] To decrease the mesoscale variability, we have subsequently spatially smoothed the data by running averaging over boxes of dimension 6°in longitude and 3°in latitude. The data are further high-pass filtered in time to retain periods shorter than 2 years, and consequently have little energy at periods outside of the 40 day to 2 year band. Figure 2 displays the root-mean-square (RMS) SSH thus processed, defined as $\sqrt{\sum_1^N \eta^2/(N-1)}$, where $N = 513$ is the number of weekly maps of the SSH η. The SSH large-scale variations are not only much smaller than the total SSH variations but also their distribution is significantly different from one of the total SSH variations, although

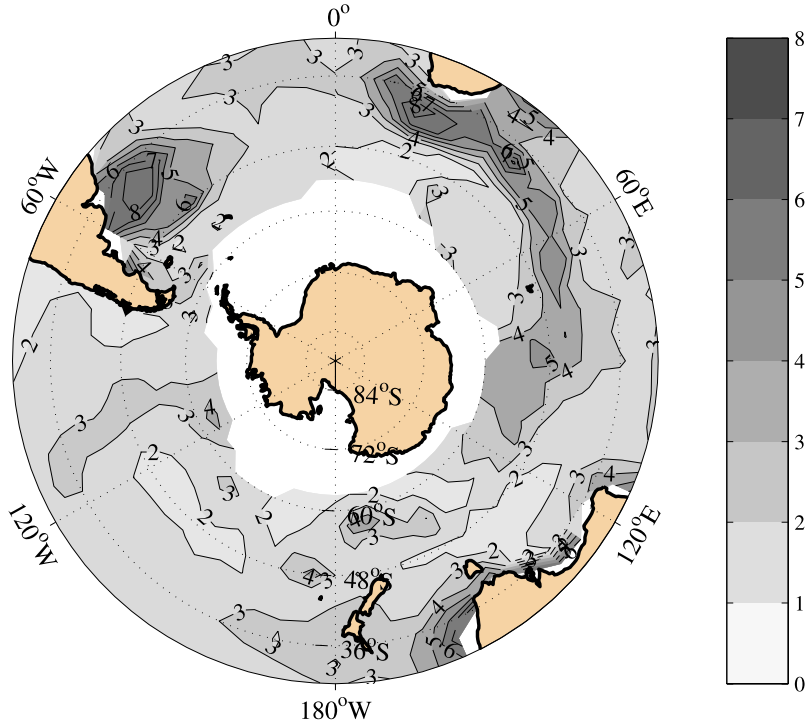

Figure 2. Root-mean-square sea surface height (SSH) from TOPEX/Poseidon and ERS for periods shorter than 2 years. Units are cm. The white area indicates the maximum extent of ice cover.

much of the regions with relatively high variability (RMS in excess of 3 cm) are still frontal zones with intense eddy activity (~25% of the initial variance is retained), such as the Brazil-Malvinas confluence, the Aghulas current retroflexion, the ACC in the Indian sector and south of New Zealand, or the East Australian current region. A thin coastal band of high variability on the south shores of Australia is associated with the boundary flow [*Ridgway et al.*, 2002]. Another band along the Patagonian shelf is likely caused by tidal aliasing. Besides these, a large fraction of the remnant variability is potentially owed to the barotropic ocean's response to winds, especially in two regions identified as resonant [*Fukumori et al.*, 1998; *Webb and de Cuevas*, 2002a, 2002b], that is, the Bellingshausen Basin, west of Drake Passage and the Antarctic-Australian Basin.

[16] A principal component analysis of the SSH reveals that almost half of the variance is accounted for by 3 modes, for which the corresponding principal components are dominated by an annual cycle (Figure 3). The leading

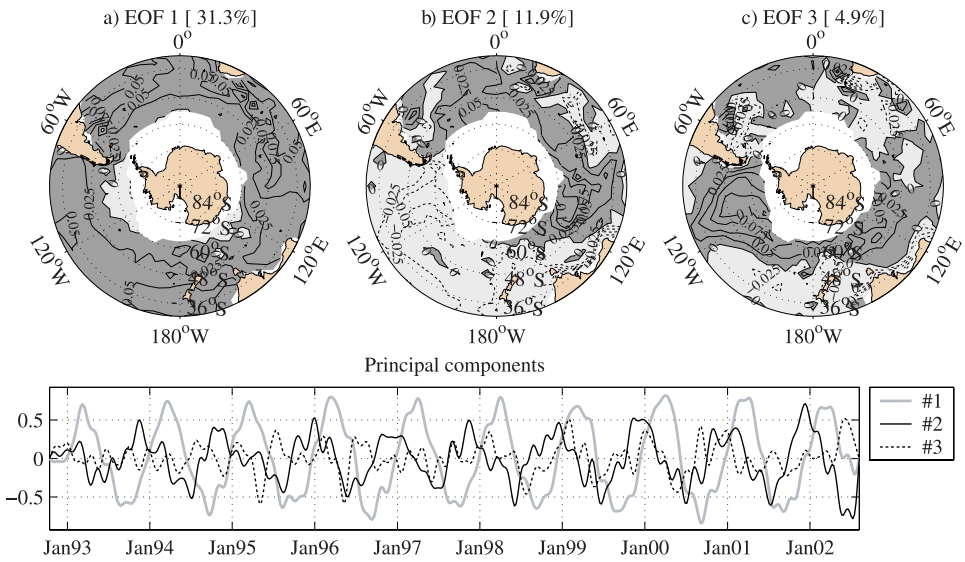

Figure 3. Principal component analysis of T/P SSH. Modes 1–3 are shown.

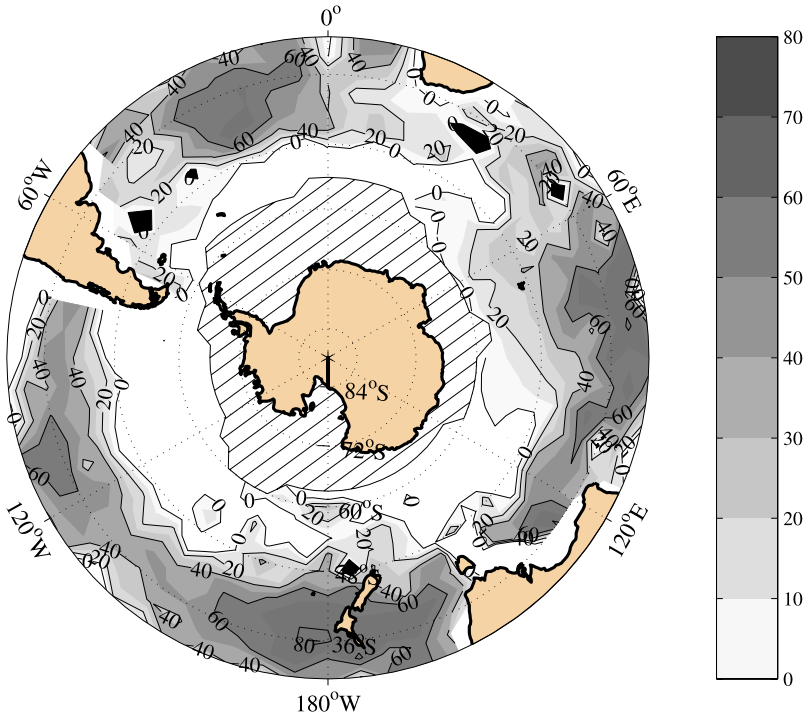

Figure 4. Skill of the thermosteric height change in accounting for altimeter SSH variance (in %).

EOF accounts for 31% of SSH variance and is zonally uniform to first order (albeit more marked in the western boundary regions) but larger at midlatitudes (30–40°S). Its corresponding principal component is almost a single annual harmonic, peaking during austral fall, hence clearly indicative of a steric height change due to seasonal heating of the ocean, as will be seen in section 3. EOFs 2 and 3, which total 17% of the SSH variance, appear to include barotropic variability (they are both enhanced south of 45°S, and in regions confined by topographic features, identified as resonant regions for the barotropic mode), mixed with seasonally modulated mesoscale variability downstream of the Kerguelen plateau for mode 2 or in the Aghulas Retroflection or Argentine Basin for mode 3. EOF2 displays an opposite phase between the signal in the Bellingshausen Basin and that in the Antarctic-Australian Basin, while these are in phase in EOF3.

2.2. Surface Fluxes

[17] In the following analyses, both momentum and heat fluxes are needed at the air-sea interface. We have used products from the new reanalysis project ERA-40 from the European Centre for Medium-Range Weather Forecasts (ECMWF), which covers the period from 1957 to August 2002. It is based on the IFS model (Integrated Forecasting System), in a version with a T159 resolution (∼120 km) and with 60 vertical levels. A variety of observations are assimilated using a three dimensional variational technique including observations from several satellites and in particular wind measurements from ERS after 1991. We have used momentum and thermal fluxes produced every 6 hours to compute 7 day averages, centered on the T/P dates, of the surface wind stress τ and of the net heat flux (turbulent plus radiative) to the ocean, denoted Q_{net}.

3. Impact of Baroclinic Processes on the SSH Variance

3.1. Steric Height Change

[18] The large-scale steric response to heat fluxes is a dominant contribution to the SSH variability at the seasonal timescale [e.g., *Gill and Niiler*, 1973; *Stammer*, 1997; *Vivier et al.*, 1999]. Following the approach described in VKT99, we estimate the steric contribution η_{steric} on the basis of a one-dimensional heat budget of the upper water column: $\partial\eta_{\mathrm{steric}}/\partial t \approx \alpha Q_{\mathrm{net}}/\rho_0 c_p$, where $\alpha(x, y, t)$, ρ_0, and $c_p(x, y)$ are the coefficient of thermal expansion in the mixed layer, mean density, and specific heat of seawater, respectively. These terms have been estimated using climatological surface temperature and salinity fields from the World Ocean Atlas 98 [*Antonov et al.*, 1998]. The steric response is largest north of 45°S (2 cm RMS on average), reaching 3 cm RMS in the Pacific Ocean. This signal accounts for a substantial fraction of T/P SSH variance (60 to 80%) north of 45°S in all three oceans (Figure 4). In Figure 4, the fraction of variance, or estimation skill, is defined as $S = 100 \times (\langle\eta^2\rangle - \langle(\eta - \eta_{\mathrm{steric}})^2\rangle)/\langle\eta^2\rangle$. We note that in the Pacific Ocean, the skill of the steric signal gradually diminishes north of 35°S because of the presence of quasi annual baroclinic Rossby waves generated at the South American coast, as was shown for instance by VKT99 using a simple kinematic model assimilating T/P data. This is also observed in the Indian Ocean north of 35°S, a region dominated by baroclinic Rossby waves [*Birol and Morrow*, 2001]. South of 45°S despite a substantial seasonal cycle in

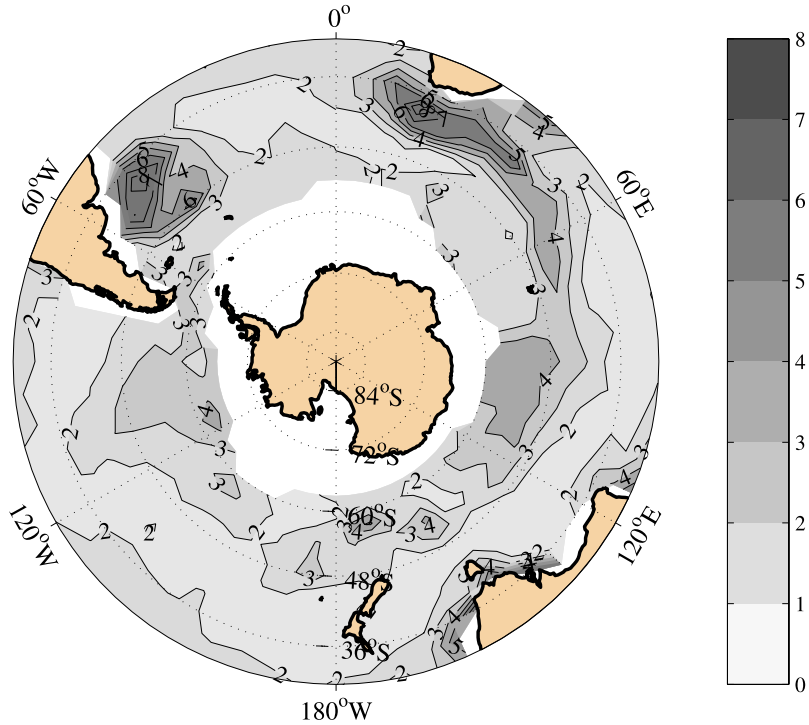

Figure 5. Root-mean-square residual SSH after correction for the steric height change. Units are cm.

the neat heat flux, the steric signal remains small, because the thermal expansion coefficient decreases greatly with water temperature [see, e.g., *Fukumori et al.*, 1998; VKT99].

[19] The standard deviation of the high-passed altimeter SSH after removal of the steric processes is shown in Figure 5. North of 40°S the remaining SSH variability of ~2 cm RMS is primarily due to baroclinic Rossby waves (VKT99). Besides this, except for regions of strong mesoscale activity mentioned earlier, most of the residual variance is seen at high latitude, suggesting barotropic processes. These are examined in section 4. We note however that because the Rossby deformation radius varies with latitude, uniform spatial smoothing applied to SSH variability does not separate baroclinic and barotropic processes in the same way for low and high latitudes. At high latitudes a large fraction of the residual variance is barotropic because baroclinic processes, which have shorter spatial scales, were more effectively removed by spatial averaging (these actually contribute most of the total SSH variability within the two major ACC frontal zones).

[20] Another process affecting the surface heat content, hence the SSH, is the heat flux due to Ekman transport across isotherms. The latter can be simply estimated as

$$\frac{\partial \eta_{\mathrm{EKtrans}}}{\partial t} = \frac{\alpha}{\rho_0 f} \boldsymbol{\tau} \times \nabla T, \qquad (2)$$

where the sea surface temperature T comes from the ECMWF archive (which assimilates satellite observations). This term is largest in frontal regions, where the temperature gradient is strongest, but even there, the RMS of η_{EKtrans} does not exceed 7 mm, while it reaches a couple of millimeters elsewhere (not shown). This term has therefore little influence at the spatial and temporal scales considered here.

[21] Surface fluxes of freshwater are another potential source of seasonal variability of the SSH in the Southern Ocean. This halosteric height change was estimated from the ECMWF precipitation and evaporation ($P - E$) data, and turned out to be negligible in the extratropics (a typical seasonal cycle has an amplitude of a few millimeters). However, owing to the lack of appropriate data, we could not estimate the halosteric contribution associated with the cycle of formation and melting of sea ice. This process is likely to be more important than the contribution of $P - E$. For instance, *Park et al.* [1998] find that the major cause of the summertime freshening of the surface layer in the Enderby Basin is the eastward advection of meltwater originating from the Weddell Basin.

3.2. Simplified Baroclinic Response to the Wind Forcing

[22] Although the baroclinic response to the wind is expected to be small at high latitude from scaling arguments, we examine whether some of the SSH variance can be explained by vertical thermocline motions due to Ekman pumping, a process that is responsible for a significant fraction of the annual variability at specific locations in the Pacific Ocean (VKT99). This response is given by $\eta_{\mathrm{EKpump}}/\partial t = g'/(\rho_0\, g)\mathrm{curl}(\boldsymbol{\tau}/f)$, where g' is the reduced gravity. The RMS amplitude of η_{EKpump} is on the order of 5 mm, but can be locally larger (1 cm), such as near the Chilean coast, where the wind stress curl is particularly large. We note however that the magnitude of this term is directly proportional to g'. The value $g' = 0.02$ m s^{-2} chosen here is canonical for the subtropics [e.g., *Flierl*, 1978], and is therefore an upper bound for the more weakly stratified

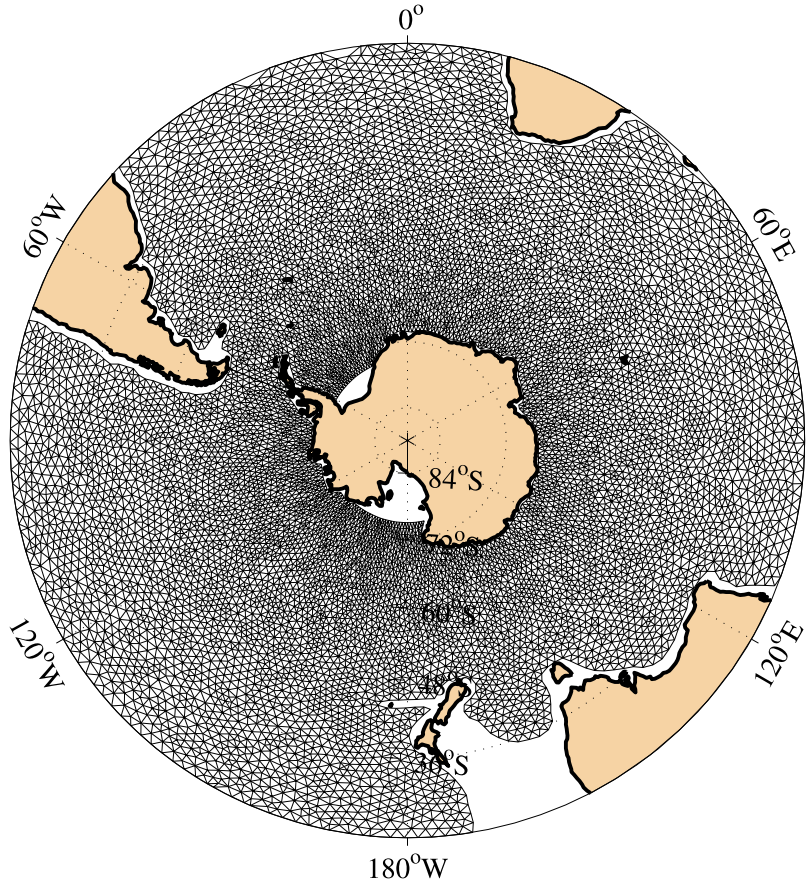

Figure 6. Triangular mesh over the Southern Ocean, treated as a periodic channel with a northern boundary linking Africa, Australia, and America at 25°S and a southern boundary at 75°S.

Southern Ocean. This suggests that Ekman pumping has only a marginal influence on the SSH variability in the Southern Ocean at seasonal timescales.

4. Barotropic Response to the Winds

4.1. Finite Element Barotropic Model Formulation

[23] Assuming a linear, hydrostatic, incompressible flow, and ignoring the baroclinic pressure torque (the so-called JEBAR term), the vorticity equation for the depth integrated flow reads (see Appendix A)

$$\nabla\cdot\frac{\nabla\psi_t}{H}-\frac{f}{H}\eta_t+\mathcal{J}\left(\psi,\frac{f}{H}\right)+\nabla\cdot\left(\frac{r}{H^2}\nabla\psi\right)=\mathrm{curl}\left(\frac{\boldsymbol{\tau}}{\rho_0 H}\right), \tag{3}$$

where subscript t denotes the time derivative, and r is the bottom friction coefficient. A relationship between ψ and η is needed to solve (3) which is provided by the geostrophic approximation

$$\frac{f}{H}\nabla\psi=g\nabla\eta. \tag{4}$$

A straightforward way to decouple the problem is to assume that f/H varies on spatial scales that are large compared with those of ψ, which yields $\eta = f/(gH)\psi$. This is however not justified in the context of the Southern Ocean and it is thus more accurate to solve the following additional equation (obtained from $\nabla\cdot(4)$) together with (3)

$$\nabla^2\eta=\nabla\cdot\left(\frac{f}{gH}\nabla\psi\right). \tag{5}$$

While we here solve the coupled problem (3)–(5), an acceptable trade-off would be to substitute $\eta = f/(gH)\psi$ into (3), solve for ψ, and ultimately compute η from (5).

[24] Equations (3) and (5) are solved over a circumpolar domain spanning 75°S to 25°S. The domain is taken as a periodic, circumpolar, channel with only two boundaries: a southern boundary at the Antarctic continent, and a northern boundary that links South America, Africa, Australia and New Zealand, closing all three oceans at 25°S. The choice of 25°S appears remote enough not to affect critically the model results in the Southern Ocean. Bathymetry is from the ETOPO5 database subsequently smoothed to retain spatial scales larger than 1°. All islands within the domain have been artificially lowered to a depth of 200m except for Tasmania, Chatham Islands, Malvinas Islands and Madagascar, which are connected to the northern boundary (Figure 6). As described in Appendix B, the weak form of (3) and (5) is solved on a finite elements mesh made of about 20000 triangles. The model resolution is therefore 1° on average (smaller at high latitudes; see Figure 6).

[25] For the sake of simplification, let us consider for a moment the stationary version of (3), which is uncoupled. This "periodic channel" configuration has been used in several analytical studies of the ocean's barotropic response in a zonal channel [*Krupitsky and Cane*, 1994; *Krupitsky*, 1995; *Wang*, 1994; *Wang and Huang*, 1995]. To solve this elliptic equation, Dirichlet boundary conditions (i.e., constant ψ, or "no flow") are assumed both at the southern and northern boundaries. Without loss of generality, $\psi_N = 0$ is assumed at the northern boundary while $\psi_S = T$, which is then the circumpolar transport, is imposed along the southern boundary. Boundary conditions are more simple for (5). If we assume ψ to be known over the domain, η is readily obtained to within an integration constant. To remove this singularity of the problem, we impose η to be zero at the northern boundary. Thus to completely solve the problem (3)–(5) with associated boundary conditions, we are left with estimating the circumpolar transport T.

[26] The relationship between the circumpolar transport of the ACC and the wind forcing has been the subject of heated debate in recent years, in particular whether the former is proportional to the wind stress ($\boldsymbol{\tau}$) or alternatively to the wind stress curl (curl($\boldsymbol{\tau}$)). The consensus of recent studies is that the ACC is not in Sverdrup balance, that is, that there is no proportionality between the transport and curl($\boldsymbol{\tau}$). Rather, the ACC is more sensitive to the zonally integrated wind stress $\overline{\tau_x}^x$ [e.g., *Tansley and Marshall*, 2001, and references therein].

[27] Even in the barotropic framework, the circumpolar transport T, which occurs primarily along unblocked f/H contours (hence on a quite different pathway than the ACC), is not a simple function of $\boldsymbol{\tau}$ or curl($\boldsymbol{\tau}$). Because flow is able to recirculate freely along unblocked circumpolar potential vorticity contours, T needs to be determined from an additional constraint, which is provided by the momentum equation. Zonally integrating the zonal momentum equation (see (A9) in Appendix A) at any latitude within the latitude range of the Drake Passage (and noting the pressure or SSH continuity) gives, in dimensional units,

$$\oint_{\text{Drake}} \left(-\frac{f}{H}\partial_x\psi - \frac{r}{H^2}\partial_y\psi \right) dx = \oint_{\text{Drake}} \frac{\tau_x}{\rho_0 H}\, dx. \qquad (6)$$

Note that, as shown in Appendix A, even for the nonstationary problem, transient terms are not retained in this equation, because this would demand to also include the $O(\epsilon)$ divergent transport field for consistency.

[28] Expression (6) provides an additional condition on ψ but does not explicitly give the circumpolar transport needed to solve (3). An elegant way to proceed is to take advantage of the linearity of the equations [e.g., *Krupitsky and Cane*, 1994], solving instead the two following boundary value problems:

[29] 1. A "forced solution" ψ_F: We first solve the problem with actual forcing, but imposing a zero circumpolar transport, that is $\psi = 0$ both at the northern and southern boundaries.

[30] 2. A "free mode" ψ_L: We then solve (3) without forcing, but imposing instead a unit circumpolar transport, that is, $\psi = 0$ at the northern boundary and $\psi = 1$ at the southern boundary.

[31] The total solution ψ is then a linear combination of the two previous solutions:

$$\psi = \psi_F + T\psi_L. \qquad (7)$$

Using (6), an expression for the circumpolar transport T is obtained, which is valid at any latitude within the latitude range of Drake Passage,

$$T = -\frac{\oint_{\text{Drake}} \frac{\tau_x}{\rho_0 H} + \frac{f}{H}\partial_x\psi_F + \frac{r}{H^2}\partial_y\psi_F\, dx}{\oint_{\text{Drake}} \frac{f}{H}\partial_x\psi_L + \frac{r}{H^2}\partial_y\psi_L\, dx}. \qquad (8)$$

[32] As is visible from (8), T will clearly depend on $\overline{\tau_x}^x$, but also on the detail of the free and forced solutions, hence indirectly on curl($\boldsymbol{\tau}$) (see the discussion by *Hughes et al.* [1999, section 2]). Although the influence of $\overline{\tau_x}^x$ is predominant, as has been evidenced in observations [*Hughes et al.*, 1999; *Gille et al.*, 2001], T is the result of a complex integral balance between forcing, transients, and dissipation.

[33] Although barotropic Rossby waves are fast (several meters per second for the fastest), the zonal extent of the Southern Ocean is such (>22000 km) that even on timescales on the order of a few months, barotropic adjustment might not have been reached, as will be verified in section 5. Moreover, for regions of closed contours, nonstationary terms are likely to be important on a wider range of frequencies. These terms are therefore retained in the vorticity equation (3), which is treated in the spectral domain, following, for example, *Greatbatch and Goulding* [1989]. Fourier transforming (3) yields

$$\nabla\cdot\left(\left(\frac{i\omega}{H}+\frac{r}{H^2}\right)\nabla\hat{\psi}\right) - i\omega\frac{f}{H}\hat{\eta} + \mathcal{J}\left(\hat{\psi},\frac{f}{H}\right) = \text{curl}\left(\frac{\hat{\tau}}{\rho_0 H}\right), \qquad (9)$$

where the carets denote Fourier transforms, and ω is the angular frequency. The condition at the southern boundary $\hat{\psi}_S = \hat{T}$ now depends on ω. As discussed in Appendix B, there are several differences between equation (9) and its stationary counterpart: the friction coefficient is here complex, and there is an additional term in the vorticity equation, $-i\omega f/H\hat{\eta}$ (which is included as a "mass" matrix in the finite element formulation), that requires to solve the coupled system including

$$-\nabla\cdot\left(f/(gH)\hat{\psi}\right) + \nabla^2\hat{\eta} = 0. \qquad (10)$$

[34] All fields involved in the vorticity equation are real, with Fourier transforms bearing properties of Hermitian symmetry: $\hat{\tau}(-\omega) = \hat{\tau}(\omega)^\dagger$, where † is the complex conjugate. Equations (9)–(10) are therefore solved for half of the spectrum (positive frequencies), which is completed by complex conjugation. After the problem has been solved for $\hat{\psi}_F$ and $\hat{\psi}_L$, and that $\hat{T}$ and $\hat{\psi}$ are estimated, time series of ψ are obtained after an inverse discrete Fourier transform. The latter is injected into (5) to get η.

4.2. Simulations

[35] The barotropic model is run for 10 years (October 1992 through August 2002), forced with 7 day averaged

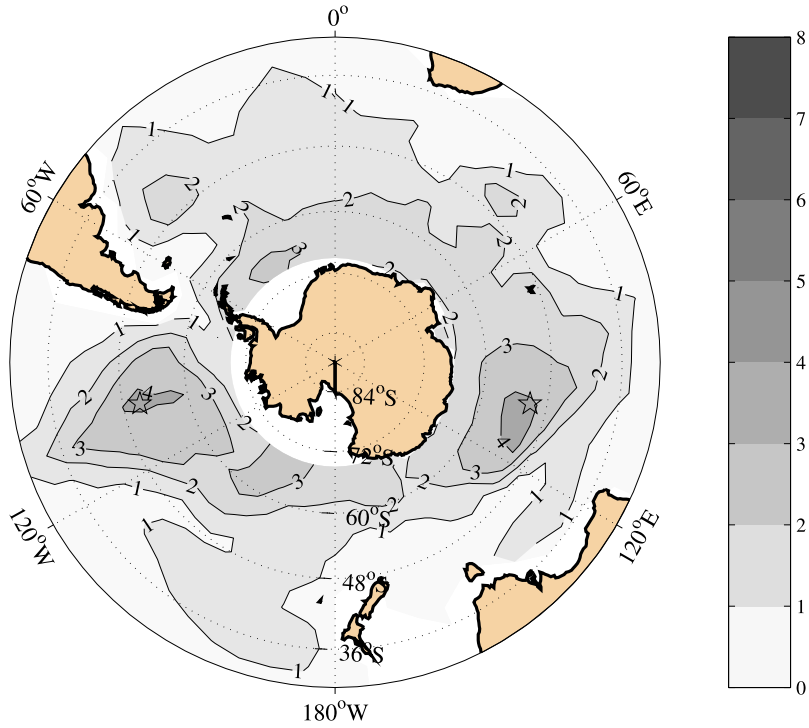

Figure 7. Standard deviation of η_{mod}, the barotropic SSH from the model (cm). The stars are the locations of the time series plotted in Figure 8.

winds (centered on T/P dates) from the ERA40 reanalysis project at the ECMWF. The barotropic SSH, denoted η_{mod}, is subsequently band-pass filtered to match T/P data processing, retaining periods between 50 and 730 days. Including the highest frequencies of the wind forcing (i.e., using 4 times daily forcing instead of weekly averages) has no influence on the band-pass-filtered outputs.

[36] The friction parameter has been tuned to 2.5×10^{-3}m s^{-1}, so as to attenuate numerical discontinuities (for the given mesh resolution). For a typical depth of 4000m, the corresponding spin-down time is ~20 days, consistent with the estimates given by *Fu* [2003]. We note that the friction parameter has only a small influence on the circumpolar transport. A stationary version of the model was run with several values of r, ranging from 1.25×10^{-3} to 5×10^{-3} yielding a circumpolar transport ranging from 25 to 24 Sv (Sv = 10^{-6} m^3 s^{-1}), while the same set of experiments for a flat bottom yielded transport ranging from 625 Sv to 190 Sv, illustrating the importance of the topographic form drag in controlling the transport. However, for larger friction coefficients, the transport becomes progressively linearly controlled by friction as in the flat bottom case.

[37] The barotropic SSH η_{mod} reaches 4 cm RMS and is largest at high latitudes (Figure 7). Figure 7 has some similarities, south of 40°S with the map of residual SSH variance after removal of the steric signal (Figure 5), with regions of enhanced variability in the Bellingshausen Basin and Australian-Antarctic Basin. In these two regions, the model is in excellent agreement with T/P data (Figure 8), with a correlation coefficient of 0.90 and 0.88 respectively (the 95% significance level is 0.17).

[38] The skill of η_{mod} in accounting for T/P SSH variance is shown in Figure 9. In the regions above, the model accounts for more than 60% of the variance. η_{mod} also present significant skill in other large regions of the Southern Ocean, such as in the South Atlantic or in the Pacific, east of New Zealand. Areas of negative skill correspond to regions where other processes dominate the SSH (e.g., eddy activity; see section 2.1) but also indicate a mixed performance of the model over shallower regions such the Pacific-Antarctic Ridge. For this region the modeled barotropic response is significantly correlated with T/P SSH (Figure 10), but the amplitude is slightly overestimated, hence the negative skill. While the barotropic SSH from the model is significantly correlated with altimeter observations over most of the domain, the area north of 45°S and located between 0°and 70°E, the area south of New Zealand and Tasmania (130–180°W) and the Drake Passage region are clear exceptions (Figure 10). The strong eddy activity associated with the retroflexion of the Aghulas current and the ACC (which is still 3–6 cm RMS despite spatial smoothing (Figure 2)), together with the small amplitude of the barotropic response (<1 cm RMS according to Figure 7), are possible reasons for the lack of skill of the barotropic model there.

[39] The result of a principal component analysis of η_{mod} is displayed in Figure 11. The leading mode, which accounts for most of the variance (41%) is predominately annular, and is trapped near the Antarctic continent. There is no such mode apparent in the EOF analysis of altimeter data (Figure 3), even after removal of the steric signal (not shown). This is for the most part due to the fact that the magnitudes of this mode are largest in areas that are masked here as being poleward of the maximum extent of sea ice. The second and third EOFs of η_{mod}, which all together account for 35% of the variance, have similarities with the second and third EOF of Figure 3 (the resemblance is much

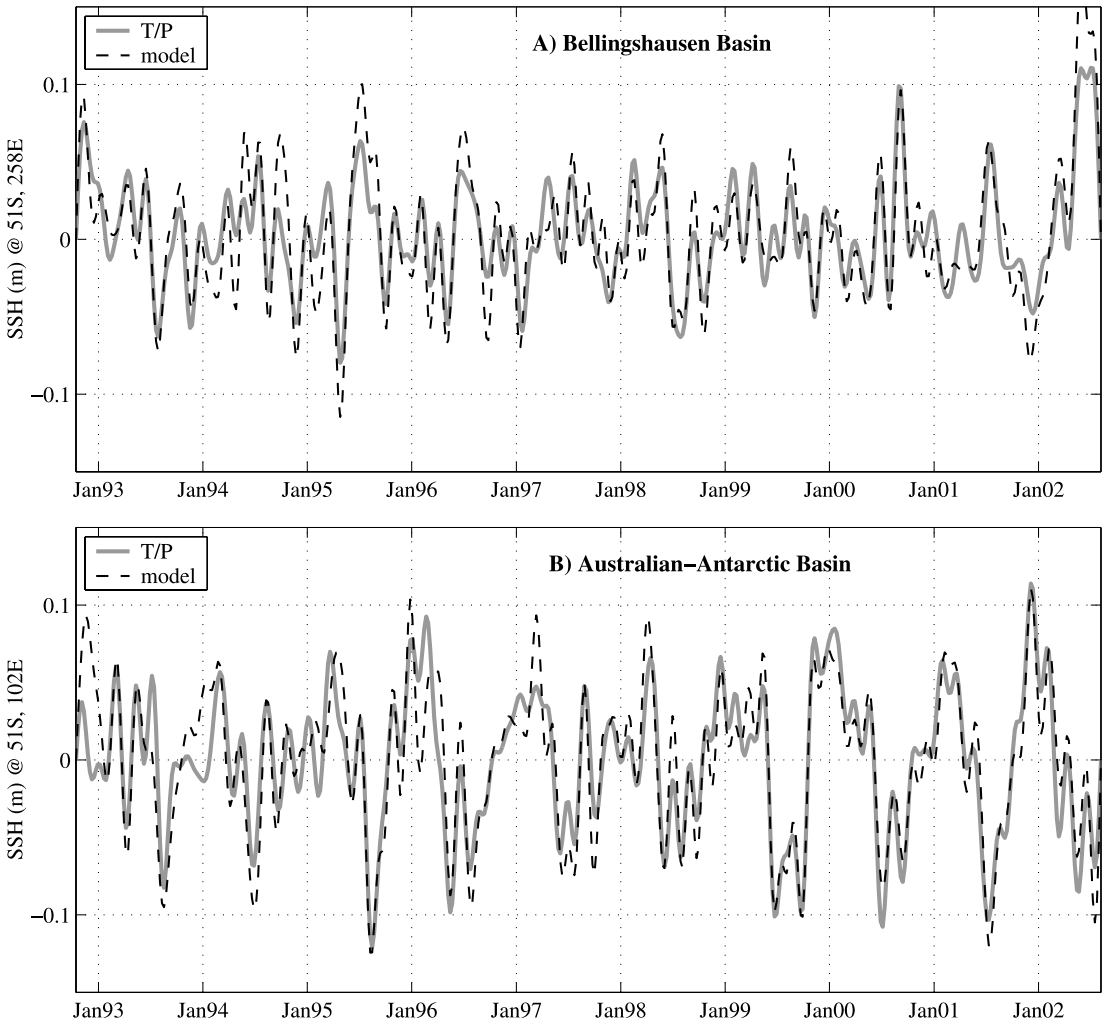

Figure 8. Time series of the SSH from T/P (solid gray lines) and from the model (dashed lines) at (a) 51°S and 258°E and (b) 51°S and 102°E.

improved by applying the same ice mask to $\eta_{|\mathrm{mod}}$ prior to the EOF analysis; not shown).

5. Leading Barotropic Dynamics

5.1. Vorticity Budget: Spectral Analysis

[40] A previous study by *Fu* [2003] has demonstrated that a simplified vorticity budget, involving a three-term balance (dissipative, transient and forcing terms) was skillful in representing the barotropic SSH variations over the Bellingshausen and Australian-Antarctic basins. Here we extend this analysis to the whole Southern Ocean by examining a detailed vorticity budget (including advection) at different timescales, a task facilitated by the barotropic model being spectral in time. In the following we estimate the relative magnitude of four contributions to the vorticity balance (3): the transient (or nonstationary) terms $\nabla \cdot \frac{\nabla \psi_t}{H} - \frac{f^2}{gH^2}\psi_t$, the advective term $\mathcal{J}(\psi, \frac{f}{H})$, the diffusive term $\nabla \cdot (\frac{r}{H^2}\nabla\psi)$, and the forcing term, curl $\left(\frac{\tau}{\rho_0 H}\right)$.

[41] Figure 12 displays the ratio of the power spectral density of the advective, diffusive and transient terms above to the forcing term, respectively, averaged over three frequency bands: high frequencies (periods from 15 to 50 days), intermediate frequencies (periods from 50 to 200 days), and low frequencies (200 to 800 days). For high frequencies, Figure 12 shows that over most of the domain, the forcing is balanced by the sum of advective and transient terms, indicative of a forced topographic wave equation. In some specific regions such as the eastern South Pacific, or eastern South Indian sector, north of 50°S, the latter two terms balance each other (red in Figure 12 indicates that both terms are an order of magnitude larger than the forcing), suggesting free (i.e., nonlocally forced) topographic waves as the leading source of barotropic SSH variance. In the intermediate and low-frequency band, the global picture is different, with a dominant vorticity balance between forcing and advection (topographic Sverdrup balance). For the 200–800 day band, transient terms play virtually no role in the vorticity budget, while dissipation becomes locally important.

[42] However, local barotropic vorticity budgets can significantly depart from this general picture, owing to the local configuration of *f*/*H* contours. This is in particular the case at the two locations studied by *Fu* [2003], denoted by circles in Figure 12, corresponding to maxima of the SSH

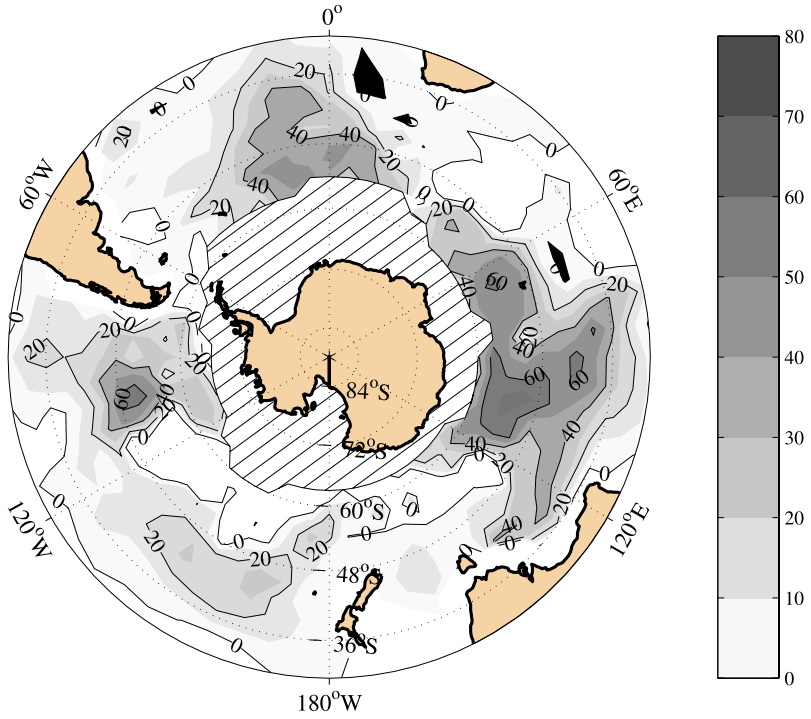

Figure 9. Skill of the SSH from the barotropic model in accounting for the T/P SSH variance (in %).

variance in the Bellingshausen Basin and the Australian-Antarctic Basin, where he could skillfully hindcast the SSH variations while neglecting the Jacobian term (advective term). According to Figure 12, in the 50–200 day band, these are indeed two locations where both dissipative and transient terms have a magnitude comparable to that of the forcing, and where the advective term is not dominant. Focusing on the intraseasonal variability (i.e., after removing all Fourier components with a period longer than 1 year as well as the semiannual harmonic), *Fu* [2003] reports a correlation of 0.5 and 0.47, respectively (with a 95% significance level of 0.2) between model and observations; however, including advection boosts these correlations to 0.72 and 0.6, respectively (the correlation is 0.9 according to Figure 8 if we include all periods shorter than 2 years), demonstrating that even in these regions advection is significant.

5.2. Coherence With the Winds: Southern Mode and Local Basin Modes

[43] To analyze the way the SSH responds to the wind forcing, we systematically examine the correlation and the coherence between η_{mod} and both $\boldsymbol{\tau}$ and curl($\boldsymbol{\tau}$).

[44] We first examine the correlation with the zonally integrated wind stress ($\overline{\tau_x}^x$) in the latitude range of Drake Passage (54°–63°S). Figure 13a exhibits a circumpolar pattern of strong negative correlation trapped near Antarctica that resembles the leading barotropic mode of variability (41% of the variance) displayed in Figure 11. As visible in Figure 11, this pattern is closely shaped by the bundle of f/H contours that circle Antarctica.

[45] In the vicinity of Antarctica, η_{mod} is much influenced by the southern boundary condition $\psi = T$, the circumpolar transport, determined by (8). As discussed in section 4, this equation shows that T is closely related to $\overline{\tau_x}^x$; that is, an increased eastward wind stress will increase the circumpolar transport; hence the observed correlation (the negative correlation with the SSH near Antarctica in Figure 13a stems from the fact that ψ and η_{mod} have opposite sign in the Southern Hemisphere).

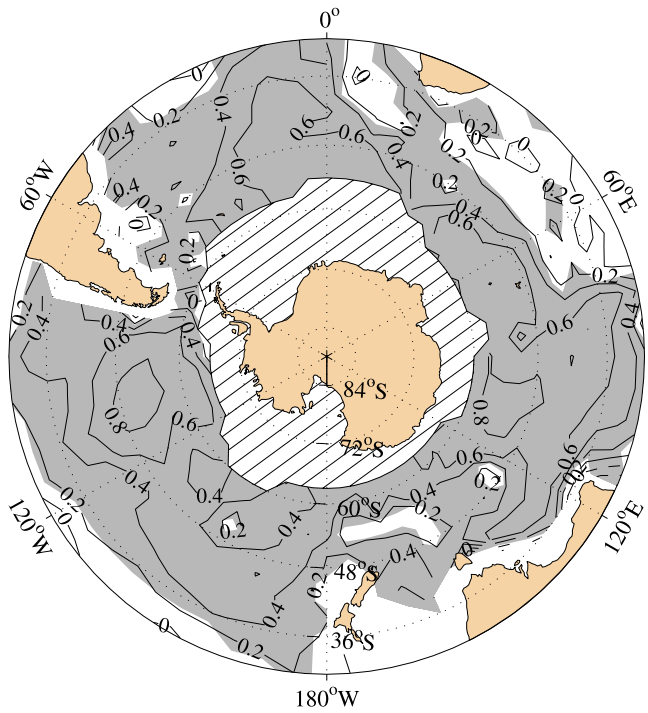

Figure 10. Correlation coefficient between the SSH from the barotropic model and from T/P. Values significant at 95% are shaded.

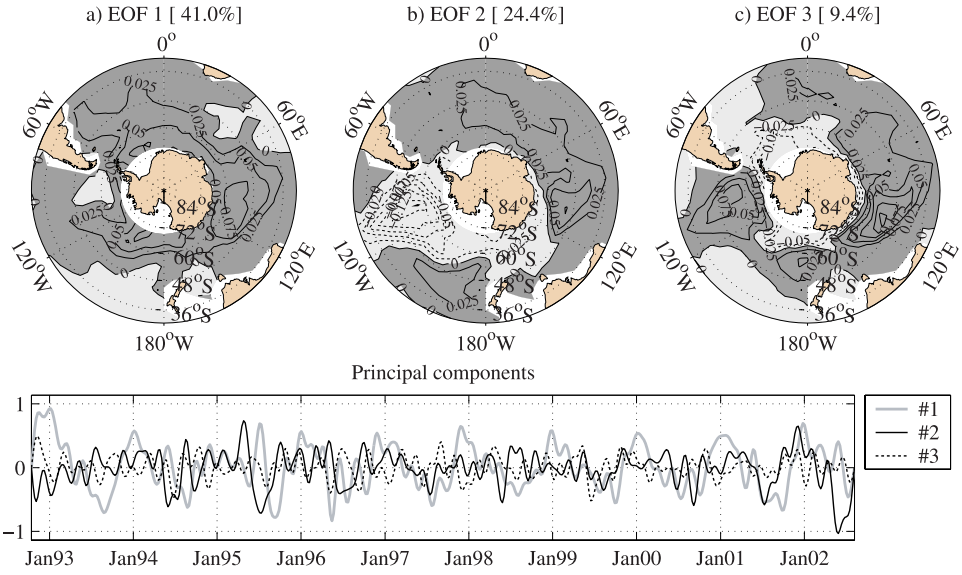

Figure 11. Principal component analysis of the SSH simulated by the barotropic model. Modes 1–3 are shown.

[46] This circumpolar mode of variability was recently discovered in different in situ measurements. It was evidenced on bottom pressure recorders (BPRs) on the southern side of Drake Passage, and has been termed the "southern mode" [*Hughes et al.*, 1999]. These pressure data, related to barotropic transport fluctuations at Drake Passage, exhibit coherence with $\overline{\tau_x}^x$. This mode was later shown to be zonally coherent from coastal gauges around Antarctica [*Aoki*, 2002] and BPRs [*Hughes et al.*, 2003], responding to the Antarctic Oscillation (AAO) [*Gong and Wang*, 1999] also known as the Southern Annular Mode (SAM) [*Thompson and Wallace*, 2000]. The eastward wind stress variations are indeed highly correlated with the AAO index. In these studies, a negative correlation is found between the eastward wind stress and the sea level (or bottom pressure) near Antarctica, consistent with the scenario that an increased (decreased) Ekman transport to the north will produce a sea level drop (rise) around Antarctica, hence an increased (decreased) circumpolar transport.

[47] *Aoki* [2002] restricted his study to the 10–100 day band, while *Hughes et al.* [1999] find coherence in the 10–220 day band, consistent with the results of *Gille et al.* [2001], who find coherences between 10 and 256 days. A similar type of response is also expected from interannual-to-centennial timescales [*Hall and Visbeck*, 2002] although at these timescales, changes in Ekman divergence affect the baroclinic structure of the ACC. Here significant coherences are found at all periods ranging from 70 days to 2 years, and in two narrow bands at 20 days and 35 days (not shown; the spatial pattern of coherence is similar to the correlation pattern of Figure 13a). However, we note that the coherence increases sharply around the semiannual period, in the 150–220 day band, reaching 0.9 (the 95% significant level is 0.4). A possible reason for a drop of coherence at periods shorter than 70 days is an increased fraction of SSH variance owed to transients. Indeed, although transient terms are not explicitly included in the integral momentum equation (6) used to determine the southern boundary condition, they nonetheless implicitly affect T through the forced solution ψ_F in (8).

[48] Model results show that this mode is clearly barotropic, in agreement with the findings of *Hughes et al.* [2003]. Figure 13a suggests that, although intensified near Antarctica, this mode has also a significant meridional extension above topographic features that connect to Antarctica, in particular above the Pacific-Antarctic Ridge, continuing up to the East Pacific Rise, where it expands up to midlatitude. A closer look at Figure 13a indicates that this mode does not straddles these ridges in a symmetric way; rather the southern mode appears intensified on their eastern flank. This appears quite clearly for the Southeast Indian Ridge, the Pacific-Antarctic Ridge, and the Kerguelen Plateau (only the souheastern tip of the plateau is encompassed in the southern mode pattern).

[49] Figure 13b shows the correlation coefficient between $\overline{\tau_x}^x$ and the SSH measured by altimetry. As mentioned in section 4.2, it is difficult to see the southern mode in the altimeter data given the ice coverage. Nonetheless, this mode can be distinctly identified in altimeter data north of 62°S, in the South Pacific basin, as an area of negative correlation. Finding weaker anticorrelations with T/P SSH than with η_{mod} is not surprising given that barotropic processes are not the only contributor to the variance of the SSH. This is particularly so in the pathway of the ACC, where the eddy activity is still an important contribution to the SSH variance despite the spatial averaging (section 2.1). This is a plausible reason why the southern mode is not so clearly apparent in the altimeter data in the region between Drake Passage and the Scotia Arc, on the Kerguelen Plateau south of 48°S or on the South East Indian Ridge, where Figure 13a indicates that it extends equatorward of the ice limit. These region are indeed local maxima in eddy activity along the ACC fronts (variations larger than 15 cm RMS in high-resolution altimeter data; not shown).

[50] Because the spatial pattern associated with this barotropic mode is primarily shaped by unblocked f/H

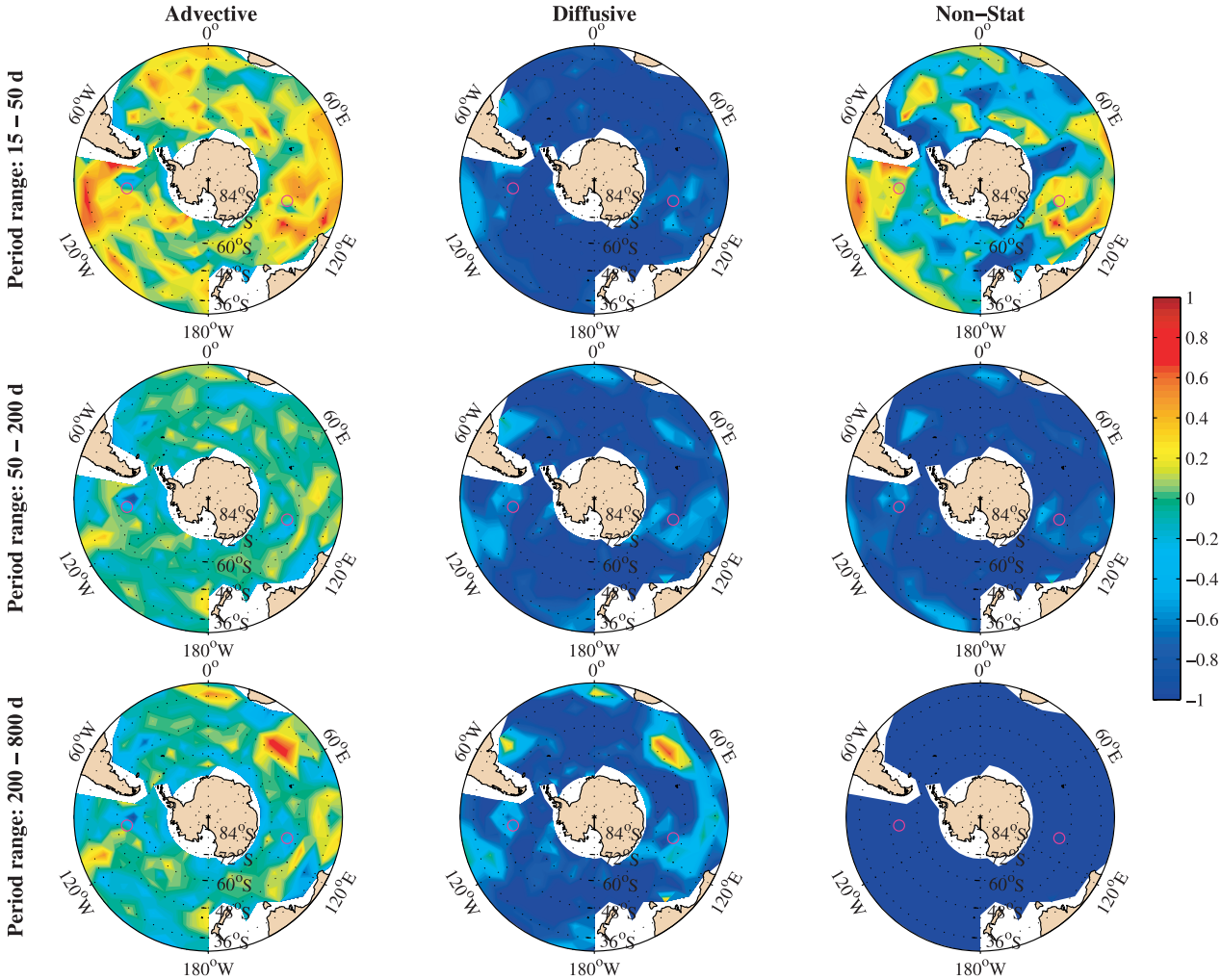

Figure 12. Ratio of the power spectral densities of terms of the vorticity budget to the forcing term: (left) advection, (center) diffusion, and (right) transient. The ratios are averaged over three different period ranges: (top) 15–50 days, (middle) 50–200 days, and (bottom) 200–800 days. The decimal logarithm is shown for clarity: Red (blue) indicates a power spectral density 10 times larger (smaller) than that of the forcing. Circles indicate the two locations in the Bellingshausen and Australian-Antarctic basins discussed in the text.

contours, it is quite different from the path of the ACC, which, because of stratification, is less sensitive to topography. This could explain why *Gille et al.* [2001] found a less clear relationship between $\overline{\tau_x}^x$ and the altimeter SSH difference across the path of the ACC than between $\overline{\tau_x}^x$ and BPR measurements to the south of Drake Passage. Indeed, in many regions (particularly the South Atlantic and Indian sectors), the mean ACC pathway is north of the area delimited by the southern mode. Accordingly, *Meredith and Hughes* [2004] find no causal correlation between $\overline{\tau_x}^x$ (or equivalently the SAM index) and BPR data at Kerguelen Island (49°S, 70°E), and conclude that this site is not well adapted to monitor the circumpolar transport. From Figure 13a, we see that this site (denoted by a star) is located just outside of the southern mode pattern, which confirms their finding.

[51] Although the southern mode accounts for more than 40% of the total barotropic SSH variance over the Southern Ocean, according to the EOF analysis shown in Figure 11, it is confined to the southernmost fraction of the domain. The ocean's response to the winds north of this zone is affected by topographic features, which separate different basins (see modes 2 and 3 in Figure 11). We now examine to what extent the ocean's response in these different basins is locally forced, by analyzing the relationship between η_{mod} and curl($\boldsymbol{\tau}$).

[52] Figure 14 (left) displays the squared coherence between η_{mod} and the local wind stress curl averaged over the high (15–50 days), intermediate (50–200 days), and low (200–800 days) frequency bands defined above. The barotropic SSH is significantly coherent at 99% with the local curl($\boldsymbol{\tau}$) in a limited number of regions, corresponding schematically, for most of them, to deep basins that are isolated by nearly closed *f*/*H* contours. Two of these regions have been recognized as resonant regions: the Bellingshausen Basin and Australian-Antarctic Basin [e.g., *Chao and Fu*, 1995; *Fukumori et al.*, 1998; *Webb and de Cuevas*, 2002a; *Fu*, 2003], with a SSH variance in excess of 4 cm RMS

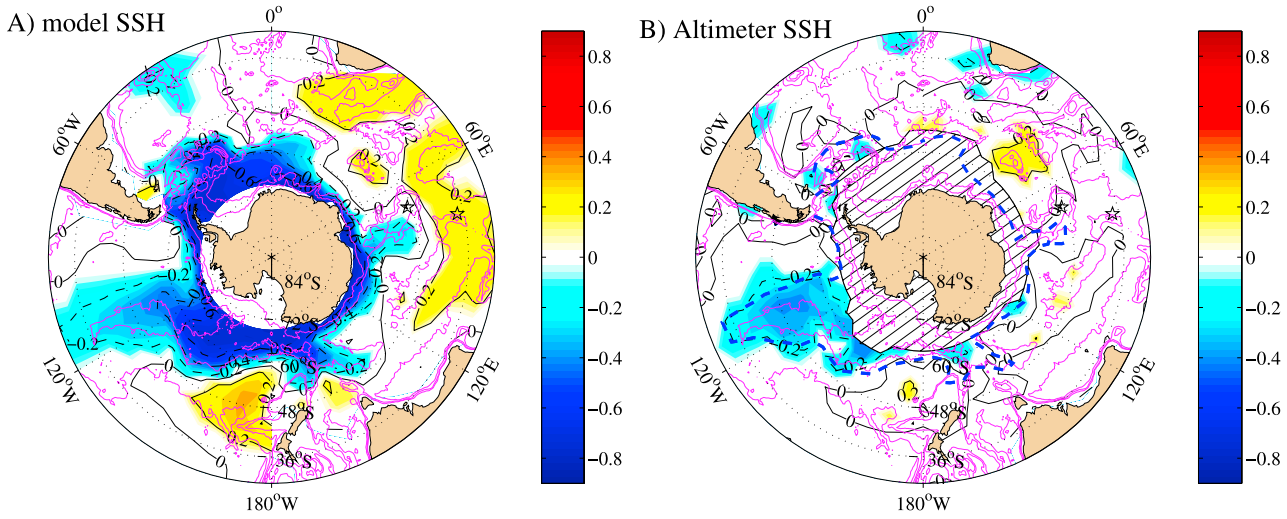

Figure 13. Correlation coefficient between the zonally integrated wind stress $\overline{\tau_x}^x$ and (a) η_{mod} and (b) the altimetric SSH. Only values significant at the 95% confidence level are displayed. Pink lines indicate f/H contours. The dashed blue line demarcates the area where the anticorrelation between η_{mod} and $\overline{\tau_x}^x$ is significant at the 99% confidence level, a region mostly covered by ice (hatched surface). The two stars indicate Kerguelen and Amsterdam islands discussed in the text.

(Figure 7). For the Australian-Antarctic Basin, however, a closer look at Figure 14 reveals that the main area of significant coherence for all 3 frequency bands is located on its northern flank (i.e., above the Southeast Indian ridge, a shallower area where f/H contours are closed), while a secondary area of coherence (for intermediate and high frequencies) is located on the deep part of the basin. This suggests that the main factor for a coherence between the ocean's response and the local forcing to be observed, is whether or not the region (deep or shallow) is enclosed by f/H contours. For an enclosed region, a coherence with the forcing can be explained by the fact that an input of vorticity by the winds will force flows inside the contours, creating a local change in the SSH. Whether the response will be resonant depends on the adequation between spectral characteristics of the forcing, the basin geometry, and dissipative timescales [*Willebrand et al.*, 1980; *Fukumori et al.*, 1998].

[53] Additional regions of coherence are found in all sectors of the Southern Ocean. In the Pacific sector these include the area north of the Bellingshausen Basin, the western South Pacific basin, and the Tasman Sea (although the artificial closure of this basin at 36°N in the model is likely to modify the ocean's response). Further west, we find the South Australian Basin and the Cape Basin west and south of Cape of Good Hope (note however that barotropic skill is small in this region, Figure 10). In the Atlantic sector, the Argentine Basin is also a region of coherence, together with regions between the Kerguelen Plateau and the Scotia Arc south of 50°S (i.e., Enderby and Weddell Abyssal plains). We note that these regions of significant coherence with curl($\boldsymbol{\tau}$) tend globally to remain as such for all frequency bands (with a tendency to expand for increasing period). The analysis of the phase spectrum (right plots of Figure 14) indicates that the phase decreases from $\sim\pi/5$ (curl($\boldsymbol{\tau}$) leading), for high frequencies down to zero for the low-frequency band. An increase of the phase lag with frequency is expected because the relative magnitude of transient terms in the vorticity balance increases linearly with frequency ($i\omega$ terms in (9), which are in quadrature with the forcing). In the Bellingshausen and Australian-Antarctic basins, this positive phase lag was previously noted by *Fu* [2003]. The present analysis suggests that this result also extends to other basins significantly coherent with curl($\boldsymbol{\tau}$) in the Southern Ocean.

[54] The coherence in the Argentine Basin at all 3 timescales is interesting because it is associated with a non-negligible barotropic variance ($\sim$2 cm RMS). As far as we know, this mode has not been seen in the altimeter data (intense eddy activity dominates the variability of this region), except for a high-frequency mode at 25 days corresponding to trapped waves rotating around the Zapiola Rise (the central seamount of the Argentine Basin) [*Fu et al.*, 2001]. At seasonal timescales, the correlation between the SSH and curl($\boldsymbol{\tau}$) was indirectly evidenced through the seasonal migration of the Brazil/Malvinas front apparent in a singular value decomposition of current meter observations and local curl($\boldsymbol{\tau}$) data [*Vivier et al.*, 2001].

[55] An interesting result from the present cross-spectral analysis is that significant coherences with curl($\boldsymbol{\tau}$) are primarily seen above regions (partially) enclosed by f/H contours. This leaves vast areas of the Southern Ocean, many above topographic features, for which the relationship with the wind forcing is more obscure. We presented evidence that the sea level variability above the East Pacific Rise and the Pacific-Antarctic Ridge is correlated with the variability near Antarctica to which it connects, as part of the southern mode. Such a nonlocal barotropic response is certainly not unique in the Southern Ocean. Indeed a location can be remotely forced as long as flow can circulate freely from the forcing region along unblocked f/H contours. The curl($\boldsymbol{\tau}$) over an enclosed region will force flows inside the area, yielding a local SSH response. The SSH gradient anomaly is in turn associated with a circulation

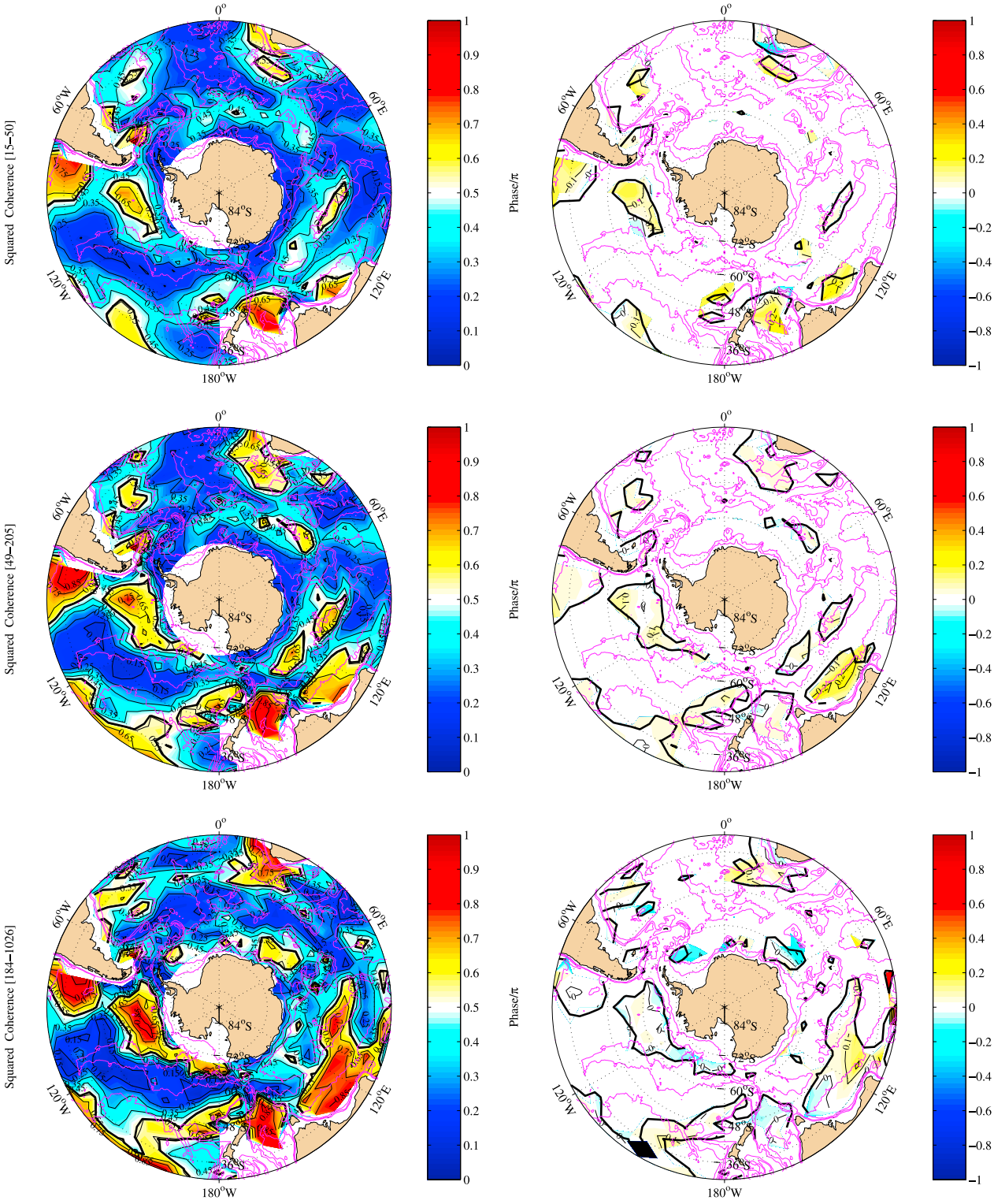

Figure 14. (left) Squared coherence and (right) phase spectra between the barotropic SSH η_{mod} and the wind stress curl. The spectra are calculated at every point throughout the domain and are averaged over three period ranges: (top) 15–50 days, (middle) 49–205 days, and (bottom) 184–1026 days. The 99% confidence level for the squared coherence (0.54) is indicated by the thick black line (the 95% significance level is 0.39). Phase maps are scaled by π, and a positive phase is curl(τ) leading. Phase is shown only for regions of significant coherence. Pink lines are f/H contours.

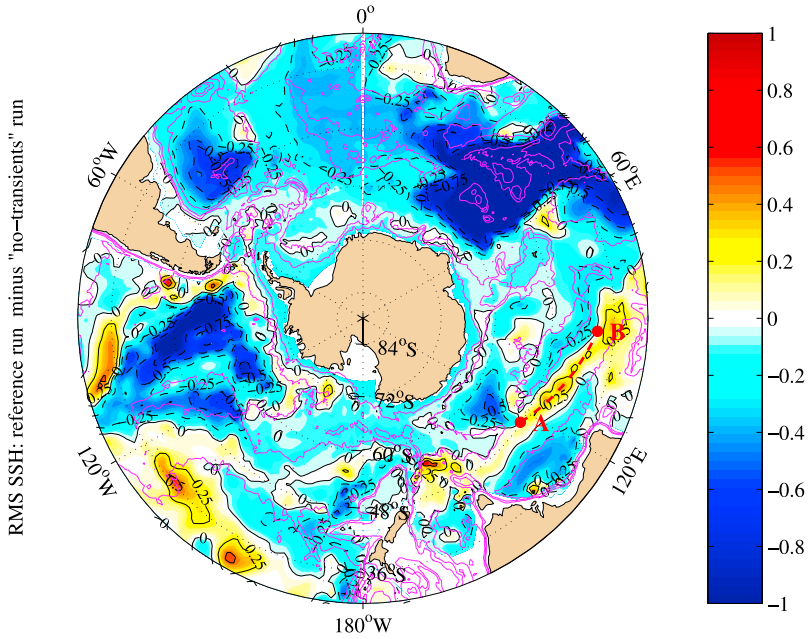

Figure 15. Impact of the transients on the barotropic SSH: difference of the RMS SSH between the reference run and the run without transients. Units are cm.

along f/H contours that circle the region, which can branch to remote locations. Another example of this process is given by the analysis of barotropic bottom pressure variations measured at Amsterdam Island (37.5°S, 77°E; denoted by a star in Figure 13) for which *Meredith and Hughes* [2004] found a correlation with curl(τ) above the Australian-Antarctic resonant basin, to which it is connected by the f/H contours that circle the Southeast Indian Ridge. Our model analyses are consistent with their results: Figure 14 shows that the barotropic SSH at Amsterdam Island is not coherent with the local curl(τ) (the region of significant coherence on the northern flank of the Australian-Antarctic basin does not extend up to Amsterdam Island); in addition, we find significant coherence between η_{mod} in this basin and at Amsterdam Island for all periods longer than 30 days (not shown). The coherence drops at higher frequencies probably owing to the influence of barotropic waves that are channeled along the northern flank of the Southeast Indian ridge (see section 5.3).

5.3. Influence of Barotropic Waves in the SSH Variance

[56] To examine the role played by transients in redistributing the energy imported by the winds we have run the model again but as a sequence of steady states (i.e., ignoring the first 2 terms of (3). Figure 15 shows the difference of the RMS SSH of the reference run minus the RMS SSH of this "no transients" run. An interesting aspect of Figure 15 is that there is generally less energy in basins identified earlier as resonant (up to 1 cm RMS) in the reference run compared to the "no transients" run. This indicates that energy is radiated away from these regions by barotropic waves. This was hypothesized by *Webb and de Cuevas* [2002a], who found a decay time of 2.6 days for the resonant mode in the eastern South Pacific, a time frame too short to involve dissipation by bottom friction. Indeed, Figure 15 clearly shows that transients convey energy along a narrow pathway of f/H contours that go around the edge of the Pacific-Antarctic Ridge. Energy seems to accumulate in the western South Pacific, or alternatively follow a narrow pathway to the south that connects to the South Indian Ocean. There is also evidence of a similar process at several different locations: north of the Australian-Antarctic Basin, a waveguide is apparent that is potentially responsible for draining energy out of this other resonant region. Another waveguide is apparent between Kerguelen and Amsterdam islands in the Indian Ocean. These waveguide regions are consistent with the "free topographic wave" regions hinted at from the spectral analysis of the vorticity budget (section 5.1).

[57] To illustrate this effect of barotropic waves, we have run the model again in the two configurations described above (with and without transients) but including higher frequencies so as to produce daily output (the forcing is also daily instead of weekly averages). This makes it possible to track individual topographic Rossby waves. The RMS difference plot is qualitatively similar to Figure 15. We have then extracted the SSH along the section AB indicated in Figure 15. Along this section there is ~40% more energy in the full run compared with the "no transient" run. A distance-time plot (Hovmoller diagram) of the SSH along this section is shown in Figure 16, for which we have removed the alongtrack mean (along section AB) to emphasize potential propagations. Figure 16a shows waves propagating northwestward from the "mouth" of the Australian Antarctic Basin (i.e., the breach in the Southeast Indian Ridge) with a phase speed of ~2 to 3. This phase speed (for which the theory indicates that it depends in particular on the wave number considered) was estimated visually and from a Radon transform of the autocorrelation matrix of the spatially demeaned SSH. It is not a surprise

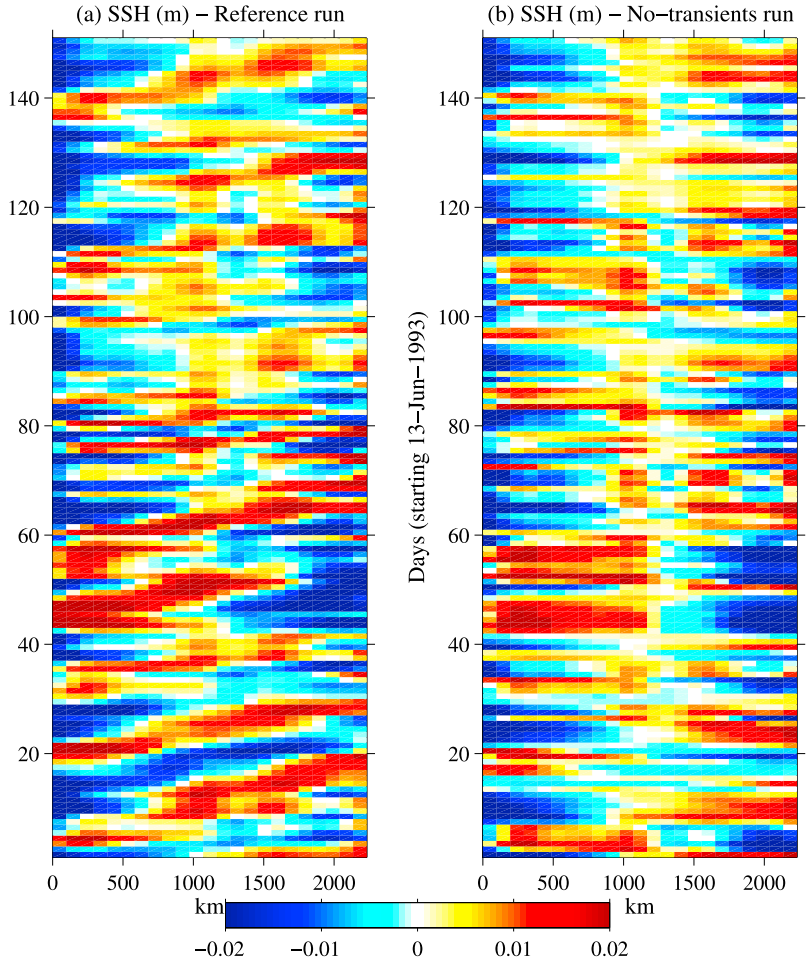

Figure 16. Hovmoller diagrams of the barotropic SSH along the northern side of the Southeast Indian Ridge (section AB is shown in Figure 15) for a high-frequency run (a) with transients and (b) without transients. The origin of distances is point A of Figure 15. At each time step, the spatial mean along the section has been removed, for both plots, to emphasize potential propagations. Units are m.

not to see such propagating features in the "no transient" run (Figure 16b). This analysis confirms that topographic Rossby waves contribute to dissipate energy from the resonant regions. Whether this mechanism dominates dissipation by bottom friction, a process supported by the analyses of *Fu* [2003], remains to be established.

[58] Finally, with have examined the effect of transients on the circumpolar transport T. While, in this linear model, the mean transport is not affected by transients, a spectral analysis (not shown) indicates that there is ∼50% more energy in the transport for the "no transient" run compared with the reference run in the 25–60 day period band (for periods longer than 60 days, differences between these two runs are marginal). This is consistent with the negative value found at the southern boundary in Figure 15. By contrast, we find less energy in the "no transient" run transport at higher frequencies (periods < 25 days), which suggests that the variability of the transport could be affected in opposite ways depending on the spectral characteristics of the waves. This analysis is however only tentative, because the momentum equation used in the determination of the transport is only O(1), and does not include explicitly transient terms (these appear implicitly through ψ_F in (8)).

6. Summary

[59] A decade of altimeter data from the T/P and ERS missions has been analyzed to document the sea surface height (SSH) variability at large spatial scales (>6°) and at timescales shorter than 2 years in the Southern Ocean, from 30°S to Antarctica. A first goal of this analysis was to be able to distinguish the different contributions to the SSH variance from different physical processes. The seasonal heat storage in the ocean, yielding thermosteric height changes is the leading contribution to the SSH variance (accounting for up to 60–80%) equatorward of 50°S, exceeding 3 cm RMS north of 45°S. By contrast, steric height changes due to horizontal advection of heat by Ekman fluxes, or caused by changes in salinity from freshwater exchanges with the atmosphere are small at these time and spatial scales.

[60] The baroclinic response to the wind forcing due to vertical Ekman pumping is also a small contribution

(<0.5 cm RMS). Instead the dominant dynamical response to wind forcing is barotropic and accounts for most of the SSH variance south of 50°S, except for regions of strong eddy activity (in the pathway of the ACC, downstream of the Aghulas retroflexion, or in the Brazil Malvinas confluence extension). In some resonant basins, the barotropic response is the largest contribution to the SSH variance up to 40°S. We note however that uniform spatial smoothing applied to SSH variability does not separate barotropic and baroclinic processes in the same way for low and high latitude. Because the internal Rossby deformation radius is shorter at high latitude, baroclinic processes are more effectively removed by spatial averaging.

[61] The barotropic response is analyzed from a numerical model forced with ECMWF winds, developed in finite elements. The modeled SSH agrees well with observations. An EOF analysis separates the variability between different regional basin modes and a circumpolar mode in the southernmost fraction of the domain. The leading empirical mode (41% of the variance of the barotropic SSH) is indeed annular and trapped near Antarctica. It is anticorrelated with the zonally integrated wind stress, consistent with a free mode response along the bundle of f/H contours that circle Antarctica. It is almost entirely responsible for the variations in the barotropic circumpolar transport. This barotropic mode is consistent with the "southern mode" evidenced in BPR data [*Hughes et al.*, 1999; *Gille et al.*, 2001; *Hughes et al.*, 2003] and coastal tide gauges [*Aoki*, 2002], shown to respond to the Southern Annular Mode. This mode is largely hidden in altimeter data because of the ice coverage, but is nevertheless distinctly identified in the in the Pacific sector where it expands meridionally above the Antarctic-Pacific Ridge and East Pacific Rise up to midlatitudes (Figure 13). The southern mode appears intensified on the eastern flank of topographic features that branch to Antarctica.

[62] The relationship between wind forcing and the ocean's barotropic response is investigated in the rest of the domain. The barotropic response is found to be coherent with curl($\boldsymbol{\tau}$) in several regions that are schematically isolated by nearly closed f/H contours, most of which are deep basins. Two of these basins (Bellingshausen and Australian-Antarctic basins) have previously been identified as resonant [e.g., *Chao and Fu*, 1995], and the barotropic SSH exceeds 4 cm RMS. The curl($\boldsymbol{\tau}$) leads the ocean's response by a lag increasing from 0 (for periods longer than 200 days) to $\sim\pi/5$ (for periods shorter than 50 days). In many regions, however, the ocean's response is nonlocal, and the forcing region can be very remote, depending on the geometry of f/H contours.

[63] A spectral analysis of the vorticity budget shows that advection balances the forcing (topographic Sverdrup balance) for periods >50 days, whereas transient and advective terms dominate at high frequencies. There are however local exceptions to this general picture, particularly in the resonant basins where the contributions of transients and diffusion are also important in the 50–200 day period band. A version of the model without transient terms was run, which demonstrated the influence of barotropic waves, channeled along f/H contours, that contribute to remove energy from resonant regions, as was hypothesized by *Webb and de Cuevas* [2002a]. Whether this is the dominant dissipative process for these basins remains to be established.

Appendix A: Derivation of the Model Equations

[64] Vertical integration of the continuity equation, using classical kinematic boundary conditions yields

$$\frac{\partial \eta}{\partial t} + \nabla \cdot [(H+\eta)\mathbf{v}] = 0. \tag{A1}$$

Denoting T, L, U f_0, and H_0 the characteristic scales for the time, horizontal distance, horizontal velocity, the Coriolis parameter, and depth, respectively, we introduce the following nondimensional numbers: $\epsilon = 1/(f_0 T)$, the Burger number Bu $= gH_0/(f_0 L)^2$, and the Rossby number Ro $= U/(f_0 L)$. The geostrophic approximation gives the following scaling for the SSH: $\eta \sim N_0 = f_0 UL/g$ (where $\sim$ means "scale like"). Hereinafter, all variables, parameters and operators are nondimensional.

[65] The nondimensional version of (A1) is

$$\frac{\epsilon}{\mathrm{Bu}}\frac{\partial \eta}{\partial t} + \nabla \cdot (\mathbf{v}H) + \frac{\mathrm{Ro}}{\mathrm{Bu}}\nabla \cdot (\mathbf{v}\eta) = 0. \tag{A2}$$

The ratio ϵ/Bu is small over most of the spectral domain considered here, but reaches O(1) for spatial scales larger than 1000 km and timescales on the order of 10 days or shorter. On the contrary, the ratio Ro/Bu is always smaller than 0.01 over the range of spatial scales considered here (i.e., larger than a few hundred kilometers), on the basis of a generous estimate of 10 cm s^{-1} for U. Therefore we neglect the Ro/Bu term in (A2).

[66] The nondimensional linearized momentum equation is

$$\epsilon \partial_t \frac{\mathbf{v}H}{H} + \frac{f}{H}\mathbf{k} \times \mathbf{v}H = -\nabla \eta - \frac{r}{H^2}\mathbf{v}H + \frac{\boldsymbol{\tau}}{H}, \tag{A3}$$

where $\boldsymbol{\tau}$ and r relate to their dimensional counterpart by multiplying by $\rho_0 f_0 H_0 U$, and $f_0 H_0$, respectively. In (A3), following *Krupitsky and Cane* [1994], we have assumed the bottom friction $\boldsymbol{\tau}_b$ to be proportional to the depth-averaged flow, that is, $\boldsymbol{\tau}_b = \frac{r}{H}\int_{-H}^{0} \mathbf{v}\, dz$.

[67] Equation (A2) shows that $\mathbf{v}H$ is nondivergent to first order and can be written in terms of a stream function ψ and a small O(ϵ/Bu) residual divergent term, that stems from a potential χ

$$\mathbf{v}H = k \times \nabla \psi + \frac{\epsilon}{\mathrm{Bu}}\nabla \chi, \tag{A4}$$

where χ can be calculated from (A2) as $\nabla^2 \chi = -\eta_t$.

[68] The vorticity equation is obtained by taking the vertical component of $\nabla\times$ (A3) substituting $\nabla \cdot (\mathbf{v}H)$ from (A2), and using decomposition (A4).

$$\epsilon \nabla \cdot \frac{\nabla \psi_t}{H} - \frac{\epsilon}{\mathrm{Bu}}\frac{f}{H}\eta_t + \mathcal{J}\left(\psi, \frac{f}{H}\right) = -\nabla \cdot \left(\frac{r}{H^2}\nabla \psi\right) + \mathrm{curl}\left(\frac{\boldsymbol{\tau}}{H}\right). \tag{A5}$$

The divergence of the geostrophic equation, $f/H\nabla\psi = \nabla\eta$, provides the following additional relation between ψ and η, needed to solve the problem

$$\nabla^2\eta = \nabla\cdot\left(\frac{f}{H}\nabla\psi\right). \tag{A6}$$

[69] The careful reader will have noted that the term $\epsilon/\mathrm{Bu}\times\nabla(f/H)\cdot\nabla\chi$ was omitted in (A5). While this is not rigorously justified since we have not assumed $\nabla(f/H)$ to be a small quantity (for example in (A6)), this nevertheless leads to considerable simplification of the numerics. In fact, a fully orthodox approach would require to solve the following vorticity equation

$$\epsilon\nabla\cdot\frac{\nabla\psi_t}{H}+\frac{\epsilon}{\mathrm{Bu}}\nabla\cdot\left(\frac{f}{H}\nabla\chi\right)+\mathcal{J}\left(\psi,\frac{f}{H}\right)=-\nabla\cdot\left(\frac{r}{H^2}\nabla\psi\right)+\mathrm{curl}\left(\frac{\boldsymbol{\tau}}{H}\right), \tag{A7}$$

while an additional relation between χ and ψ is obtained by combining (A4), (A2) and (A6), yielding

$$\nabla^4\chi = -\nabla\cdot\left(\frac{f}{H}\nabla\psi_t\right). \tag{A8}$$

Equation (A8), involving a bi-Laplacian operator, and thus additional boundary conditions on the field's derivatives is certainly more complex to solve, and is left for future improvements of the model.

[70] To solve (A5), we need to estimate the value of $\psi_S = T$ imposed at the southern boundary. For this, as discussed in section 4, we examine the momentum equation (A3), using the decomposition (A4). A careful balance of the powers of ϵ shows that unless going through the burden of estimating the $0(\epsilon/\mathrm{Bu})$ transport term $\nabla\chi$, we must drop the transient term in (A3) for a consistent equation. Hence the following O(1) zonal momentum equation.

$$\frac{f}{H}\partial_x\psi = \partial_x\eta+\frac{r}{H^2}\partial_y\psi+\frac{\tau_x}{H}. \tag{A9}$$

Zonally integrating this equation along a latitude circle, and using the decomposition (7) of section 4 gives the searched boundary condition (8) expressed in dimensional units.

Appendix B: Finite Element Formulation of the Model

[71] Let us first consider the stationary version of (3). The finite element resolution is based on the projection of the weak form of (3) onto a functional space of finite dimension. The weak form is obtained after multiplication by an arbitrary test function (denoted v) and integration over the spatial domain, denoted Ω, taking into account the conditions on the boundaries $\partial\Omega$. The derivation of the weak form can be greatly simplified by rewriting (3) as

$$\nabla\cdot(\mathbb{K}\nabla\psi) = F, \tag{B1}$$

where $F = \mathrm{curl}\,(\boldsymbol{\tau}/\rho_0 H)$, and where the symmetric part of the matrix $\mathbb{K}$ is proportional to the friction term, whereas the antisymmetric part is proportional to the potential vorticity:

$$\mathbb{K} = \begin{pmatrix} r/H^2 & -f/H \\ f/H & r/H^2 \end{pmatrix}. \tag{B2}$$

[72] The weak form is then obtained using Green-Ostrogradski's formula to drop an order of derivative, and equation (3) with its associated boundary conditions is equivalent to finding ψ such that

$$\int_\Omega -\mathbb{K}\nabla\psi\cdot\nabla v\,d\mathcal{V}+\int_{\partial\Omega} v\mathbb{K}\nabla\psi\cdot\mathbf{n}\,ds=\int_\Omega Fv\,d\mathcal{V},\quad\forall v. \tag{B3}$$

[73] The domain is divided in Nt triangles connecting Np nodes. The choice of functions ψ and v is restricted to a subspace of dimension Np, denoted V_{Np} for which we define a convenient base made of N_p piecewise linear "hat" functions $\phi_i(x, y)$ such that

$$\begin{cases}\phi_i(x_i,y_i)=1\\ \phi_i(x_j,y_j)=0,\quad\text{for } j\neq i,\ j\in[1,\cdots,Np],\end{cases} \tag{B4}$$

where (x_i, y_i) are the coordinates of node i. Consequently we can project ψ on this base $\psi(x, y) = \sum_{j=1}^{Np}\Psi_j\phi_j(x, y)$ and the problem is reduced to finding nodal values Ψ_j. Since the differential operator is linear, it is sufficient to solve (B3) for Np test functions chosen here as the base function of V_{Np} (from which any possible test function can subsequently be constructed). The problem now reduces to the following linear system:

$$\begin{cases}\sum_{j=1}^{Np}\left(\int_\Omega\mathbb{K}\nabla\phi_j\right)\cdot\nabla\phi_i\,d\mathcal{V})\ \Psi_j=\int_\Omega F\phi_i\,d\mathcal{V}\\ \text{for } i\in[1,\cdots,Np]\ \text{and}\ i\notin\partial\Omega\\ \Psi_i\ \text{imposed, for, } i\in\partial\Omega,\end{cases} \tag{B5}$$

which is solved after assembling the matrices which coefficients are defined by the integrals on the left hand side of (B5), as well as the vector at the right hand side.

[74] To ensure the zonal periodicity of the model (here at the latitude of Drake Passage) we match the indices of the nodes east and west of Drake Passage during the assembling process. Doing so, these nodes are treated like any other node in the domain interior.

[75] Once ψ is obtained, it is used as a forcing term for (5) which is solved for nodal values of η using a similar procedure as above.

[76] For the coupled time-dependent problem, formulated in the spectral domain, we instead solve the following linear coupled system for each frequency

$$\begin{cases}\mathbf{K}_1\hat{\psi}+\mathbf{M}\hat{\eta}=\hat{F}\\ \mathbf{K}_2\hat{\psi}+\mathbf{K}_3\hat{\eta}=0,\end{cases} \tag{B6}$$

where the second equation above stems from the projection of the weak form of (10) and assembling of the

corresponding stiffness matrices $\mathbf{K}_2$ and $\mathbf{K}_3$. The first equation of (B6) differs from (B5) by considering instead a complex friction coefficient $i\omega/H + r/H^2$ in $\mathbf{K}_1$ and adding a term with a mass matrix $\mathbf{M}$ ponderated with $-i\omega f/H$ coefficients.

[77] **Acknowledgments.** The altimeter products were produced by Ssalto/Duacs as part of the Environment and Climate EU Enact project (EVK2-CT2001-00117) and distributed by Aviso, with support from CNES. We are indebted to Jérôme Sirven, Young-Hyang Park, and three anonymous reviewers for their valuable comments on the manuscript. F.V. thanks CNRS and CNES for their support.

References

Antonov, J., S. Levitus, T. P. Boyer, M. Conkright, C. O'Brien, and T. D. Stephens (1998), *World Ocean Atlas 1998*, vol. 1, *Temperature of the Atlantic Ocean*, *NOAA Atlas NESDIS 27*, NOAA, Silver Spring, Md.

Aoki, S. (2002), Coherent sea level response to the Antarctic Oscillation, *Geophys. Res. Lett.*, *29*(20), 1950, doi:10.1029/2002GL015733.

Birol, F., and R. Morrow (2001), Source of the baroclinic waves in the southeast Indian Ocean, *J. Geophys. Res.*, *106*(C5), 9145–9160.

Chao, Y., and L.-L. Fu (1995), A comparison between TOPEX/Poseidon data and a global ocean general circulation model during 1992–1993, *J. Geophys. Res.*, *100*(C12), 24,965–24,976.

Collecte, Localisation, Satellites (2002), SSALTO/DUACS user handbook, version 1.1, Toulouse, France.

Cummins, P. F. (1991), The barotropic response of the subpolar North Pacific to stochastic wind forcing, *J. Geophys. Res.*, *96*(C5), 8869–8880.

Dorandeu, J., and P.-Y. Le Traon (1999), Effects of global mean pressure variations on sea level changes from TOPEX/POSEIDON, *J. Atmos. Oceanic Technol.*, *16*, 1279–1283.

Ducet, N., P. Y. Le Traon, and G. Reverdin (2000), Global high-resolution mapping of ocean circulation from TOPEX/Poseidon and ERS-1 and -2, *J. Geophys. Res.*, *105*(C8), 19,477–19,498.

Flierl, G. R. (1978), Models of vertical structure and the calibration of two-layer models, *Dyn. Atmos. Oceans*, *2*, 341–381.

Fu, L. L. (2003), Wind-forced intraseasonal sea level variability of the extratropical oceans, *J. Phys. Oceanogr.*, *33*, 436–449.

Fu, L. L., and A. Cazenave (2001), *Satellite Altimetry and Earth Sciences, A Handbook of Techniques and Applications*, *Int. Geophys. Ser.*, vol. 69, Elsevier, New York.

Fu, L.-L., and R. A. Davidson (1995), A note on the barotropic response of sea level to time-dependent wind forcing, *J. Geophys. Res.*, *100*(C12), 24,955–24,963.

Fu, L.-L., B. Cheng, and B. Qiu (2001), 25-day period large-scale oscillations in the Argentine Basin revealed by the TOPEX/Poseidon altimeter, *J. Phys. Oceanogr.*, *31*, 506–517.

Fukumori, I., R. Raghunath, and L.-L. Fu (1998), Nature of global large-scale sea level variability in relation to atmospheric forcing: A modeling study, *J. Geophys. Res.*, *103*(C3), 5493–5512.

Gill, A. E., and P. P. Niiler (1973), The theory of the seasonal variability of the ocean, *Deep Sea Res.*, *20*, 141–177.

Gille, S. T., D. P. Stevens, R. T. Tokmakian, and K. J. Heywood (2001), Antarctic Circumpolar Current response to zonally averaged winds, *J. Geophys. Res.*, *106*(C2), 2743–2760.

Gong, D., and S. Wang (1999), Definition of Antarctic Oscillation index, *Geophys. Res. Lett.*, *26*, 459–462.

Greatbatch, R. J., and A. Goulding (1989), Seasonal variations in a linear barotropic model of the North Pacific driven by the Hellerman and Rosenstein wind stress field, *J. Geophys. Res.*, *94*(C9), 12,645–12,665.

Hall, A., and M. Visbeck (2002), Synchronous variability in the Southern Hemisphere atmosphere, sea ice, and ocean resulting from the annular mode, *J. Clim.*, *15*, 3043–3057.

Hasselmann, K. (1982), An ocean model for climate variability studies, *Prog. Oceanogr.*, *11*, 69–92.

Hughes, C. W., M. P. Meredith, and K. J. Heywood (1999), Wind driven transport fluctuations through Drake Passage: A southern mode, *J. Phys. Oceanogr.*, *29*, 1971–1992.

Hughes, C. W., P. L. Woodworth, M. P. Meredith, V. Stepanov, T. Whitworth III, and A. Pyne (2003), Coherence of Antarctic sea levels, Southern Hemisphere Annular Mode, and flow through Drake Passage, *Geophys. Res. Lett.*, *30*(9), 1464, doi:10.1029/2003GL017240.

Koblinsky, C. J. (1990), The global distribution of f/H and the barotropic response of the ocean, *J. Geophys. Res.*, *95*(C3), 3213–3218.

Krupitsky, A. (1995), Local and remote forcing of the barotropic transport through a periodic gap in a basin with bottom topography, *J. Mar. Res.*, *53*, 201–210.

Krupitsky, A., and M. A. Cane (1994), On topographic pressure drag in a zonal channel, *J. Mar. Res.*, *52*, 1–23.

Le Traon, P.-Y., F. Nadal, and N. Ducet (1998), An improved mapping method of multisatellite altimeter data, *J. Atmos. Oceanic Technol.*, *15*, 522–534.

Meredith, M. P., and C. W. Hughes (2004), On the wind-forcing of bottom pressure variability at Amsterdam and Kerguelen islands, southern Indian Ocean, *J. Geophys. Res.*, *109*, C03012, doi:10.1029/2003JC002060.

Mestas-Nuñez, A. M., D. B. Chelton, and R. A. De Szoeke (1992), Evidence of time-dependent Sverdrup circulation in the South Pacific from Seasat scatterometer and altimeter, *J. Phys. Oceanogr.*, *22*, 934–943.

Park, Y. H., E. Charriaud, and M. Fieux (1998), Thermohaline structure of the Antarctic Surface Water/Winter Water in the Indian sector of the Southern Ocean, *J. Mar. Syst.*, *17*(1–4), 5–23.

Ray, R. (1999), A global ocean tide model from TOPEX/Poseidon altimetry/GOT99.2, *NASA Tech. Memo. NASA/TM-1999-209478*, 58 pp., NASA Goddard Space Flight Cent., Greenbelt, Md.

Ridgway, K. R., J. R. Dunn, and J. L. Wilkin (2002), Ocean interpolation by four-dimensional weighted least squares—Application to the waters around Australasia, *J. Atmos. Oceanic Technol.*, *19*, 1357–1375.

Rintoul, S. R., S. Sokolov, and J. Church (2002), A 6 year record of baroclinic transport of the Antarctic Circumpolar Current at 140°E derived from expendable bathythermograph and altimeter measurements, *J. Geophys. Res.*, *107*(C10), 3155, doi:10.1029/2001JC000787.

Sokolov, S., and S. R. Rintoul (2002), Structure of Southern Ocean fronts at 140°E, *J. Mar. Syst.*, *37*(1–3), 151–184.

Stammer, D. (1997), Steric and wind-induced changes in TOPEX/Poseidon large-scale sea surface topography observations, *J. Geophys. Res.*, *102*(C9), 20,997–21,009.

Stammer, D., C. Wunsch, and R. M. Ponte (2000), De-aliasing of global high frequency barotropic motions in altimeter observations, *Geophys. Res. Lett.*, *27*, 1175–1178.

Tansley, C. E., and D. P. Marshall (2001), On the dynamics of wind-driven circumpolar currents, *J. Phys. Oceanogr.*, *31*, 3258–3273.

Thompson, D., and J. Wallace (2000), Annular modes in the extratropical circulation. Part I: Month-to-month variability, *J. Clim.*, *13*, 1000–1016.

Vivier, F., K. A. Kelly, and L. Thompson (1999), Contributions of wind forcing, waves, and surface heating to sea surface height observations in the Pacific Ocean, *J. Geophys. Res.*, *104*(C9), 20,767–20,788.

Vivier, F., C. Provost, and M. P. Meredith (2001), Remote and local forcing in the Brazil/Malvinas region, *J. Phys. Oceanogr.*, *31*, 892–913.

Wang, L. (1994), A linear homogeneous model for topographic control of the Antarctic Circumpolar Current, *J. Mar. Res.*, *52*, 649–685.

Wang, L., and R. X. Huang (1995), A linear homogeneous model of wind-driven circulation in a β-plane channel, *J. Phys. Oceanogr.*, *25*, 587–603.

Webb, D. J., and B. A. de Cuevas (2002a), An ocean resonance in the southeast Pacific, *Geophys. Res. Lett.*, *29*(8), 1252, doi:10.1029/2001GL014259.

Webb, D. J., and B. A. de Cuevas (2002b), An ocean resonance in the Indian sector of the Southern Ocean, *Geophys. Res. Lett.*, *29*(14), 1664, doi:10.1029/2002GL015270.

Willebrand, J., S. G. H. Philander, and R. C. Pacanowsky (1980), The oceanic response to large-scale atmospheric disturbances, *J. Phys. Oceanogr.*, *10*, 411–429.

M. Harismendy and F. Vivier, Laboratoire d'Océanographie Dynamique et de Climatologie, Institut Pierre Simon de Laplace, Université Pierre et Marie Curie, 4 Place Jussieu, F-75252 Paris cedex 05, France. (fvi@lodyc.jussieu.fr)

K. A. Kelly, Applied Physics Laboratory, University of Washington, 1013 NE 40th Street, Seattle, WA 98195, USA.